2022

THE VARIABILITY OF THE SATURATION RATIO IN CLOUDS

Jesse C. Anderson
Michigan Technological University, jcanders@mtu.edu

THE VARIABILITY OF THE SATURATION RATIO IN CLOUDS

By

Jesse C. Anderson

A DISSERTATION

Submitted in partial fulfillment of the requirements for the degree of

DOCTOR OF PHILOSOPHY

In Atmospheric Sciences

MICHIGAN TECHNOLOGICAL UNIVERSITY

2022

This dissertation has been approved in partial fulfillment of the requirements for the Degree of DOCTOR OF PHILOSOPHY in Atmospheric Sciences.

Department of Physics

Dissertation Advisor:	*Dr. Will H. Cantrell*
Committee Member:	*Dr. Raymond A. Shaw*
Committee Member:	*Dr. Mike Larsen*
Committee Member:	*Dr. Caroline Jarrold*
Department Chair:	*Dr. Ravindra Pandey*

Dedication

To Natalie Anderson & Daniel Gregory Anderson

Contents

List of Figures

List of Tables

Acknowledgments

As I am nearing the end of my graduate student career, I am filled with nostalgia. There are so many people who have helped me along my journey and I am incredibly thankful. Without the support, camaraderie, and occasional tough love from everyone, I would not be where I am today. I sincerely hope I have improved your lives as much as you have improved mine.

I am grateful for having the opportunity to work with Dr. Will Cantrell. You have been an excellent role model and mentor from me the moment I arrived at Tech.

I would like to thank my committee members, Dr. Raymond Shaw, Dr. Mike Larsen and Dr. Caroline Jarrold. Dr. Shaw, you have been great resource for me in my development as a scientist.

Thank you Prasanth Prabhakaran for the MANY discussions which were instrumental in this dissertation and my studies.

I would like to thank Laura Fierce for your help during my time working virtually at PNNL under the U.S. Department of Energy, Office of Science, Office of Workforce Development for Teachers and Scientists, Office of Science Graduate Student Research (SCGSR) program. Additionally, I would like to thank Mikhail Ovchinnikov, Fan

Yang, Payton Beeler, and Steven Krueger, for the fruitful discussion and contributions my work during the SCGSR program.

Thank you to David Ciochetto, Greg Kinney, and Ian Helman for your help teaching me how to use the chamber, and fixing my mistakes.

Thank you to all of the people who have helped me along the way: Abu Sayeed Md Shawon, Subin Thomas, Kamal Kant Chandrakar, Tim Wagner, Andrew Puyleart, Tyler Capek, Kevin Waters, Lisa Eggart, Elise Rosky, Susanne Glienke, Nithin Allwayin, Shreya Joshi, Nurun Nahar Lata, Neel Desai, Janarjan Bhandari, Susan Mathai, Jaemin Yeom, Sarita Karki, Eduardo Rodriguez-Feo, and Dennis van der Voort.

Abstract

The saturation ratio determines the growth of cloud droplets by condensation and activation of aerosol particles. In a uniform environment, the interactions between the saturation ratio and cloud droplets are well understood. However, the presence of turbulent mixing causes spatial and temporal variability in the temperature, water vapor and the saturation ratio. When applied to a cloud, the variability in S has been shown to broaden the cloud droplet size distribution through each droplet having its own growth rate and history. When droplets grow by condensation or evaporation, water vapor and heat feedback with the environment, altering the distribution of the saturation ratio.

This dissertation explores the nature of the variability in the saturation ratio in clouds using measurements and simulations of the Michigan Tech Π chamber. Measurements of the Π chamber show the Large Scale Circulation contributes to the variability of the saturation ratio. We have found the saturation ratio has significant fluctuations in both moist and cloudy conditions. Increasing the concentration of cloud condensation nuclei was shown to decrease the mean saturation ratio, however the variance was unchanged. Using a box model alongside the high resolution simulation of the Π chamber, we found fluctuations in the saturation ratio cause aerosol particles to

activate in mean subsaturated conditions. We show turbulent fluctuations in the supersaturation increases the concentration of cloud condensation nuclei, by increasing the efficiency of aerosol activation.

Chapter 1

Introduction

Clouds have long been known to have a large impact on the weather and Earth's climate [1, 2]. The radiative properties and precipitation potential of a cloud are determined by the size and concentration of cloud droplets [3, 4, 5]. Cloud droplets in a warm cloud grow through two processes: condensation and collision-coalescence. Both growth mechanisms are impacted by turbulent mixing in the atmosphere. This dissertation will explore two different consequences of turbulence in warm clouds: What is the variability of the saturation ratio in clouds and how does that variability influence droplet growth and activation?

1.1 Turbulence

Turbulence is seen and felt everyday. We can feel it in a swirling breeze or when jostled in an airplane. We can see it when cream is poured into coffee, smoke rises from a fire, in the art of Van Gogh, and in the shapes of clouds. Despite being ever-present in our lives, representing the chaotic motion of turbulence and its effects is challenging. Turbulence is characterized by eddies with a large variety of scales. Large scale motions, such as updrafts, affect areas of $\sim$1 km, while small scale motions are on the scale of $\sim$ 1mm. Understanding cloud processes at the scale of a droplet is difficult due to uncertainties in cloud microphysics, and the broad range of aerosol sizes and compositions. The smallest scales of cloud physics cannot be resolved by current earth system models and cloud scale large eddy simulations [6].

1.1.1 Rayleigh-Bénard convection

Thermal convection is one of the many causes of turbulence. One specific type of convection used to model the atmospheric boundary is Rayleigh-Bénard convection (RBC). In RBC two horizontal parallel plates are separated by a distance, H. An unstable temperature gradient is set up between the plates, where the bottom plate is heated and the top plate is cooled [7]. For convection to begin, the buoyancy force

must overcome the viscous damping of the air, which is often described using the dimensionless Rayleigh number. The Rayleigh number is [8]:

$$Ra = \frac{\alpha g H^3 \Delta T}{\kappa \nu}, \tag{1.1}$$

where ν is the kinematic viscosity, ΔT is the temperature difference between the plates, α is the coefficient of thermal expansion and κ is the thermal diffusivity. Humid air has a different density than dry air of the same temperature, which affects the buoyancy of a parcel. When moisture is taken into account for convection, the Rayleigh number can be expressed as [8]:

$$Ra = \frac{\alpha g H^3 \Delta T}{\kappa \nu} + \frac{g \epsilon \Delta r H^3}{\kappa \nu}, \tag{1.2}$$

where $\epsilon \equiv \frac{m_d}{m_v} - 1$, m_d is the molecular mass of dry air, m_v is the molecular mass of water, and Δr is difference in the vapor mixing ratio between the top and bottom plates. The water vapor mixing ratio is defined as the mass of water vapor divided by the mass of dry air.

1.1.2 Large Scale Circulation

One of the characteristics of Rayleigh-Bénard convection is the formation of a mean flow or large scale circulation (LSC), which was first described in 1981 by Krishnamurti and Howard [9]. The circulation is a result of warm and cold plumes organising into a meta-stable flow [10]. The flow forms convective cells which can be seen through measurements of the fluid velocity and/or temperature fields [11]. The organisation of these cells is determined by the aspect ratio ($\Gamma = D/H$, where D is the diameter and H is the height of the cell.) of the convective cell. At higher aspect ratios, like the atmosphere, multiple hexagonal convective rolls form [12].

For $\Gamma < 4$, only a single cell will form [12]. The single roll has an updraft and downdraft on opposite sides of the cell, with horizontal motion along the floor and ceiling. At its simplest, the fluid motion of the single roll moves in a vertical plane with an axis of rotation at the center of the cell. The orientation of the vertical plane defines the azimuthal position of the LSC. As helpful as this view is, the motion of a single roll is dynamic. Even when the azimuthal position is 'locked' due to tilting of the cell [13], the LSC oscillates in several modes. Azimuthal oscillations are ever present about a central, vertical axis [14]. A twisting or torsional mode occurs when the azimuthal oscillations at top and bottom of the cell are out of phase [15, 16]. The roll can move side-to-side along the axis of rotation causing the sloshing mode

[13, 17]. In cells where $\Gamma \gtrsim 2$, the LSC can take the form of a jump rope vortex [18, 19, 20]. In addition to the oscillating, the LSC has been shown to randomly cease and reorient [21, 22, 23, 24].

The atmospheric boundary layer (ABL) is often approximated using RBC, with the ground and the top of the boundary layer acting as the heated and cooled plates [7, 25, 26]. Similar to small convection chambers, a LSC forms in the ABL [27, 28] which is sometimes referred to as the large scale motion. The updrafts and downdrafts inherent to the large scale motion have been shown to play a key role in cloud formation [29]. As helpful as this approximation is, the behavior of downdrafts in the ABL deviates from RBC [30].

1.2 Variability in Water Vapor, Temperature, and Relative Humidity

In a turbulent environment, isobaric mixing of air parcels causes fluctuations in water vapor, and temperature, resulting in fluctuations in the saturation ratio. The saturation ratio is defined as,

$$S = \frac{e}{e_s(T)} = \frac{r}{r_s(T)} \tag{1.3}$$

where r is the water vapor mixing ratio, r_s is the saturated water vapor mixing ratio, e is the water vapor pressure and e_s is the saturated water vapor pressure. An expression for the saturated water vapor pressure is can be derived by integrating the Clausius-Clapeyron equation. However, because the latent heat of vaporization has a dependency on temperature, it is convenient to use an empirical expression for $e_s(T)$. Of the empirical formulations, the Magnus equation, is [31]:

$$e_s(T) = e_0 exp\left(A_L \frac{T - T_0}{T - B_L}\right), \tag{1.4}$$

where e_0=611 Pa, T_0=273.12K, $A_L \simeq$17.2, and $B_L \simeq$36K.

The saturation ratio determines the condensational growth rate of droplets. The mass growth rate of a cloud droplet is given by [32]:

$$\frac{dm_d}{dt} = 4\pi r_d \rho_l G\left(S - S_K\right) \tag{1.5}$$

where m_d and r_d are the mass and radius of the drop, respectively, ρ_l is the density of liquid water, S_K is the saturation ratio at the surface of the droplet, and G incorporates surface and heat transfer effects. In the simplest viewpoint (where solute effects and the curvature of the droplet are ignored), when $S > 1$ the droplet is considered

to be in a supersaturation and will grow by condensation.

In a turbulent environment, water vapor, temperature and the saturation ratio can be expressed as a sum of mean and fluctuating terms:

$$T = \overline{T} + T', e = \overline{e} + e', S = \overline{S} + S'. \tag{1.6}$$

Using these decompositions with Equation 1.3 allows for the variance in S to be expressed as a function of r' and T'. In Kulmala et al. [33], the variance in S is shown to be:

$$\sigma_S^2 = \left(\frac{\overline{e}}{e_s(\overline{T})}\right)^2 \left(\underbrace{\frac{\overline{e'^2}}{\overline{e^2}}}_{\text{A}} - \underbrace{\frac{2L}{R\overline{T}^2}\frac{\overline{e'T'}}{\overline{e}}}_{\text{B}} + \underbrace{\left(\frac{L}{R\overline{T}^2}\right)^2 \overline{T'^2}}_{\text{C}} \right). \tag{1.7}$$

In 1.7, the variance of S depends on three terms: the water vapor variance term (A), the covariance of e and T (B) and the temperature variance term (C). When the variability of e and T are increased, the variance of S is also increased. When e and T fluctuate in tandem, the covariance of e and T increases, which decreases the variance of S.

Entrainment, differences in updraft velocity and isobaric mixing of air can all cause

inhomogeneity S. The variability in S causes the individual droplets in a cloud to each experience different local values of S, which causes each droplet to experience a different growth rate. Several studies have shown S variability acts to broaden the cloud droplet size distribution [33, 34, 35, 36, 37, 38].

1.3 Motivation

1.3.1 Atmospheric Models

Climate models and cloud scale Large Eddy Simulations (LES) do not have the ability to resolve the microphysics in clouds. The highest resolution climate models have a grid-spacing $\sim$ 25km [39]. On the other hand, cloud-scale LES has a higher resolution, with grid sizes in the range of 100km-10m. Atmopheric models make up for unresolved scales by parameterizing the physics at the subgrid scale (SGS) [6, 40]. Current paramerterizations include bulk models [41, 42], bin models [43, 44, 45, 46] and Lagrangian Superdroplets [36, 47, 48]. These parameterizations are still a source of uncertainty for cloud scale models, in part because they overly simplify (or ignore) the small scale fluctuations in the saturation ratio. Recently direct numerical simulations of the Michigan Tech Π chamber have been used to benchmark new SGS models [49].

1.3.2 Laboratory and Field Measurements

Laboratory measurements may be the key towards understanding cloud microphysics. The Π chamber has been used for several years to study aerosol cloud interactions in a turbulent environment [50, 51]. In the Π chamber, fluctuations in the saturation ratio have been shown to have a significant impact on the cloud droplet size distribution [38, 51, 52] and on aerosol activation [53, 54]. Recently, the Turbulent Leipzig Aerosol Cloud Interaction Simulator (LACIS-T) has been developed to study aerosol-cloud interactions by mixing air with different temperatures and water vapor concentrations in a turbulent wind tunnel [55].

Historically measurements of S in cloudy environments have been few, each with their own limitations. A measurement of S by Gerber [56] in 1991 showed there is variability in S in fog. This measurement required the sensor to be heated when the relative humidity was greater than 100 % which likely caused a disruption in the measurement. Additionally, the response time of the sensor was 2.25 seconds, which artificially averaged out the high-frequency fluctuations of S. High frequency measurements of S in clouds were reported by Ditas et al. in 2012 and in Seibert and Shaw in 2017 [57, 58]. Despite the fast response time of these measurements, the large scale spatial variability of S is represented rather than the small scale fluctuations due to turbulent mixing. High-frequency hygrometer measurements have been made

in LACIS-T [59], however the variability of S in cloudy conditions has not yet been reported.

1.4 Outline

This dissertation contains five chapters, all of which center around the turbulent fluctuations in the saturation ratio.

Chapter 2, quantifies the large scale motion inside of the Π chamber, titled "Effects of the large-scale circulation on temperature and water vapor distributions in the Π Chamber". We use a large eddy simulation in order to estimate how spatial and temporal averaging artificially decreases the measured variability in the saturation ratio. We discuss the following questions:

† How does the large scale circulation behave in the Π chamber?

† How does the large scale circulation alter the measurements of the water vapor concentration and temperature?

† Do the statistics of the water vapor concentration, temperature and saturation ratio depend on the measurement location in the Π chamber?

Chapter 3, discusses the turbulent fluctuations in the saturation ratio. We present the

first high-speed laboratory measurement of the small scale variability in S in cloudy conditions. We discuss how the concentration of CCN impacts the variability of S.

Chapter 4 includes a description and results of a box model I developed with Laura Fierce as part of the U.S. Department of Energy, Office of Science, Office of Workforce Development for Teachers and Scientists, Office of Science Graduate Student Research (SCGSR) program. With our model we determine the role of turbulent variability in S on the activation of aerosol particles.

Chapter 5 includes a summary of this dissertation and a brief discussion about possible for future projects based off the work in Chapters 3 and 4.

Chapter 2

Effects of the large-scale circulation on temperature and water vapor distributions in the Π Chamber

This chapter details measurements of the large scale circulation in the Michigan Tech Π chamber in dry and moist convection. This work was published in its full form in Atmospheric Measurement Techniques[1][2].

[1]Anderson, J. C., Thomas, S., Prabhakaran, P., Shaw, R. A., & Cantrell, W. (2021). Effects of the large-scale circulation on temperature and water vapor distributions in the Π Chamber. Atmospheric Measurement Techniques, 14(8), 5473-5485.
[2]

2.0.1 Abstract

Microphysical processes are important for the development of clouds and thus Earth's climate. For example, turbulent fluctuations in the water vapor mixing ratio, r, and temperature, T, cause fluctuations in the saturation ratio, S. Because S is the driving factor in the condensational growth of droplets, fluctuations may broaden the cloud droplet size distribution due to individual droplets experiencing different growth rates. The small scale turbulent fluctuations in the atmosphere that are relevant to cloud droplets are difficult to quantify through field measurements. We investigate these processes in the laboratory, using Michigan Tech's Π Chamber. The Π Chamber utilizes Rayleigh-Bénard convection (RBC) to create the turbulent conditions inherent in clouds. In RBC it is common for a large scale circulation (LSC) to form. As a consequence of the LSC, the temperature field of the chamber is not spatially uniform. In this paper, we characterize the LSC in the Π chamber and show how it affects the shape of the distributions of r, T and S. The LSC was found to follow a single roll with an updraft and downdraft along opposing walls of the chamber. Near the updraft (downdraft), the distributions of T and r were positively (negatively) skewed. At each measuring position S consistently had a negatively skewed distribution, with the downdraft being the most negative.

2.1 Introduction

The effects that clouds have on Earth's climate system are quite sensitive to the details of processes that occur on scales much smaller than the cloud as a whole. For example, two clouds with the same amount of liquid water can behave differently depending upon their droplet size distributions. If the liquid water content (LWC) is distributed over a large number of small droplets the cloud will be quite reflective and unlikely to precipitate. Conversely, a cloud with the the same amount of liquid water distributed over fewer droplets will be less reflective and more likely to precipitate [3, 4, 60].

The two principal processes that shape the cloud droplet size distribution are condensation/evaporation and collision-coalescence. Condensation is driven by gradients in the saturation ratio, $S \equiv \frac{e}{e_s}$, between the environment and the surface of the droplets and can result in a rapid increase in size for small droplets. Here, e is the water vapor partial pressure and e_s is the saturation vapor pressure. However, because $\frac{dR}{dt} \propto \frac{S-1}{R}$, where R is the radius of the droplet and t is time, growth to sizes larger than $R \approx 10$ μm takes longer than the typical lifetime of most clouds [61]. On the other hand, the rate of collision-coalescence only becomes appreciable once some droplets reach a size of $R \approx 20$ μm [62, Chpt.13]. How this gap in size between growth by condensation and collision-coalescence is bridged has been one of the enduring questions in cloud

physics for the past few decades [61].

Clouds are ubiquitously turbulent, which has been suggested as a mechanism for broadening the cloud droplet size distribution. Turbulence may increase the likelihood of collisions between droplets [63]. Fluctuations in water vapor concentration and temperature due to turbulence also result in fluctuations in the saturation ratio. The variance in S implies each droplet in a cloud experiences a different growth rate, and the differing growth rates could broaden the cloud droplet size distribution [38, 51, 56, 64]. However, in the atmosphere it is difficult to quantify the fluctuations in S. (See Siebert and Shaw [58] for one example.) A laboratory setting, where the effects of fluctuations in S on activation and the drop size distribution can be quantified [51, 54, 65, 66], is one way some of the enduring questions associated with growth of cloud droplets can be addressed. (Laboratory investigations of the effect of turbulence on collision-coalescence would likely require facilities with greater vertical extents than are currently available [67].) The laboratory environment has the benefit that clouds can be formed and sustained repeatably under known boundary conditions and their properties measured in steady state conditions, which allows ample time for statistically meaningful measurements.

The laboratory facility is Michigan Tech's Π Chamber, described in Chang et al [68]. We provide a brief overview here. The chamber operates under conditions of turbulent Rayleigh-Bénard convection (RBC), where the lower surface of the cell is

set to a higher temperature than the upper surface. These conditions cause turbulent mixing due to the buoyancy difference between warm and cool air. As the air mixes it results in fluctuations in the temperature; the nature of these fluctuations in the scalar field have been studied intensely [see *e.g.* 7, 69]. As examples, fluctuations in temperature have been shown to depend on the geometry of the convection cell, the intensity of turbulence and the working fluid.

The turbulent intensity and fluid properties are typically described using the Rayleigh number ($Ra = \frac{\alpha g H^3 \Delta T}{\kappa \nu}$) and the Prandtl number ($Pr = \frac{\nu}{\kappa}$) respectively, where g is the acceleration due to gravity, ΔT is the temperature difference between the top and bottom plates separated by distance H, α is the coefficient of thermal expansion of the fluid, κ is its thermal diffusivity, and ν is its kinematic viscosity. For a gradient in both temperature and water vapor, the Rayleigh number becomes [8]

$$Ra = \frac{\alpha g H^3 \Delta T}{\kappa \nu} + \frac{g \epsilon \Delta r H^3}{\kappa \nu} \tag{2.1}$$

where $\epsilon \equiv \frac{m_d}{m_v} - 1$, m_d is the molecular mass of dry air, m_v is the molecular mass of water, and r is the vapor mixing ratio. Note that for the range of conditions explored in this paper, Ra is dominated by the first term in Eq. (2.1). Studies of the temperature profile (statistics) on the vertical axis of cylindrical cells show a well mixed fluid with little gradient outside the boundary layer [70, 71, 72]. There are fewer studies of the off-center bulk temperature profiles (statistics) [73, 74].

In turbulent Rayleigh-Bénard convection a structure forms in the fluid flow, referred to as the "mean wind of turbulence" or large-scale circulation (LSC). It is a mean, background flow within the overall turbulent motion in the chamber. For cells that have an aspect ratio ($\Gamma \equiv D/H$, where D is the cell diameter) near one or two, the LSC usually takes the form of a single roll which spans the diameter of the chamber [12]. This single roll has an updraft on one side of the cell that has a positive mean vertical velocity and a higher temperature than the center of the chamber. Along the opposite side of the cell the fluid typically has a negative vertical velocity and lower temperatures. A visualization of the circulation is shown on the left side of Fig 2.1. For cells with $\Gamma \gtrsim 4$, multiple convective rolls become the dominant circulation mode [12]. We anticipate the circulation in the Π chamber will follow a single roll due to the chamber having $\Gamma = 2$.

The updraft-downdraft associated with the large scale circulation typically adopts a specific orientation within the cell, but also has several oscillatory modes about that mean position. One of the primary oscillations is azimuthal, about a vertical axis that runs through the center of the cell [23]. Often the azimuthal oscillation at the top and bottom of the chamber are out of phase. The resulting oscillation is called the torsional mode [16]. In addition the LSC has been shown to oscillate side to side in what has been referred to as the sloshing mode [75]. In cells with very high symmetry, the LSC can spontaneously cease and reorient to a different angular location [14, 21, 22, 24]. An asymmetry, such as tilting the cell, can fix the orientation

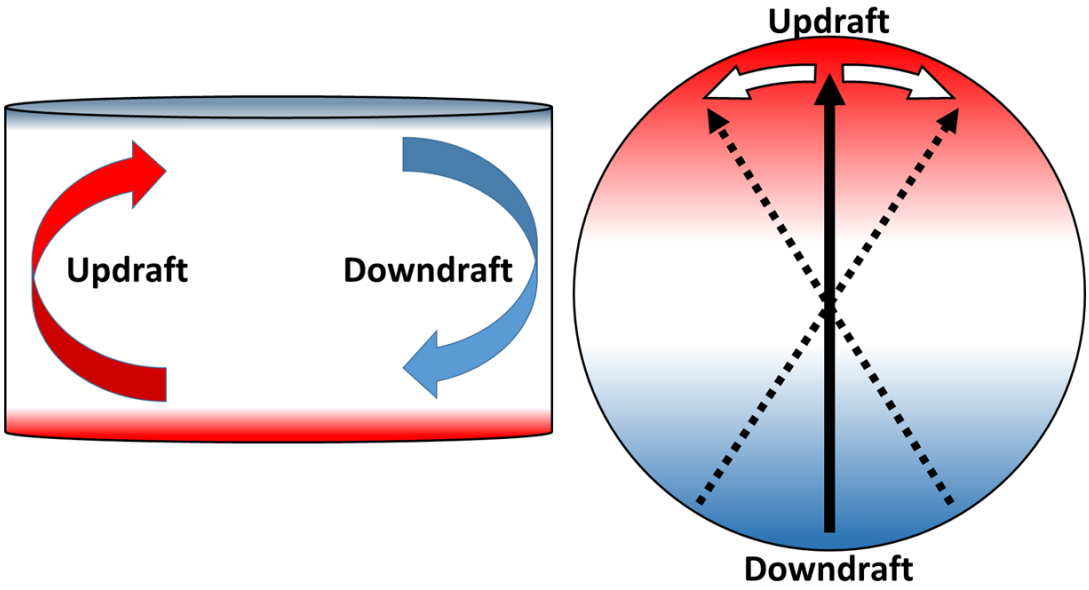

Figure 2.1: Cross section (left) and plan view (right) of the motion of the LSC in a cylindrical geometry of aspect ratio 2. On the left figure the arrows indicate the mean direction of the airflow due to the circulation with the red arrow describing the warm updraft and the blue arrow representing the cool downdraft. On the right side of the figure the black solid arrow points towards the updraft. The white arrows and dotted black arrows describe the azimuthal oscillations in the circulation.

of the LSC [13].

One of the primary motivations for studies in the Π chamber is to understand cloud microphysical processes in the atmosphere; one emphasis is determining how fluctuations in the saturation ratio affect the drop size distribution and aerosol activation. For example in [51], a zeroth order model (a stochastic differential equation) was used to quantify the effect of fluctuations in S on droplet growth. The treatment of fluctuations in temperature and water vapor concentration in the chamber was recently refined using a one dimensional turbulence model (ODT) [76], which incorporates

vertical variations. It should also be noted that a mean field approach captures many aspects of the microphysical processes in the chamber [77]. While these models have provided valuable insights into processes in the chamber, the assumption of no spatial variability or of variability in only the vertical direction comes into question in the presence of an LSC in the chamber, where the mean temperature is horizontally nonuniform. It is necessary to measure the spatial and temporal variability in r, T and S in order to determine how closely the models of reduced dimensionality capture the true variability in the chamber.

In this paper we describe the basic characteristics of the flow in the chamber, including the large scale circulation because of the importance of these quantities on the distribution of temperature and water vapor, and thus on the saturation ratio. While measurements of temperature in turbulent Rayleigh-Bénard convection are ubiquitous, as noted above, measurements of water vapor concentration are rare, and differ in some fundamental aspects from measurements of temperature. We first describe how we compare measurements of water vapor and temperature through an exploration of how a path averaged measurement differs from an ideal point measurement. Next, we describe the behavior of the LSC in the chamber across several temperature differences. We then describe how the LSC changes the shape of the temperature distributions in the bulk of the chamber. Finally we present measurements of water vapor concentration, temperature and the saturation ratio, S, at different locations in the LSC of the Π-chamber for both dry ($S < 1$) and moist ($S > 1$) convection.

2.2 Methods

2.2.1 Facility

Our experiments were conducted in Michigan Tech's Π Chamber with the cylindrical insert in place; in those conditions, $\Gamma = 2$. The cylindrical insert restricts the volume of the chamber to 3.14 m^3. To induce convection, the top and bottom control surfaces within the chamber are set such that $T_{Top} < T_{Bottom}$ and $T_{Sidewall} = (T_{Top}+T_{Bottom})/2$. In the experiments reported here, data was recorded for temperature differences ($\Delta T = T_{Bottom} - T_{Top}$) up to 16 K. These measurements are recorded at 1 Hz. The chamber is described in greater detail in Chang et al. [68].

We present measurements in two different conditions in the chamber; dry and moist convection. In our experiments the distinction between dry and moist convection is determined by the saturation ratio, S, defined as

$$S \equiv \frac{r}{r_s(T)} = \frac{e}{e_s(T)} \tag{2.2}$$

where r is the water vapor mixing ratio, $r_s(T)$ is the saturated mixing ratio which is a function of the temperature T, e is the vapor pressure and e_s is the saturation vapor

pressure. In practice, the saturation values are calculated from an empirical approximation of the Clausius-Clapeyron equation, in our case the Magnus approximation, using the measured value of T [32]. We define dry convection as a subsaturated condition ($S < 1$) in the chamber. In moist convection the chamber is supersaturated ($S > 1$), with the bottom, top, and sidewalls of the chamber being saturated. In moist conditions, a cloud would form if aerosol particles were present, but for these experiments, we did not inject aerosols into the chamber which prevents the formation of cloud droplets.

2.2.2 Instrumentation

Our basic temperature measurement is through 100 Ω, thin film, platinum resistance thermometers (RTDs, Minco, S17624, 100 Ω ± 0.12%). After calibrating the RTDs against each other in an isolated box, the difference between two RTDs was then calculated. The uncertainty was then calculated by taking the standard deviation of that difference, which was determined to be ± 0.001K). A ring of eight RTDs, 1 cm away from the wall of the cylinder was used to determine the orientation and amplitude of the large scale circulation. The RTDs are on the horizontal midplane of the chamber and are evenly spaced such that the angular distance between each one is $\pi/4$ radians. The setup for this experiment can be seen in Fig. 2.2.

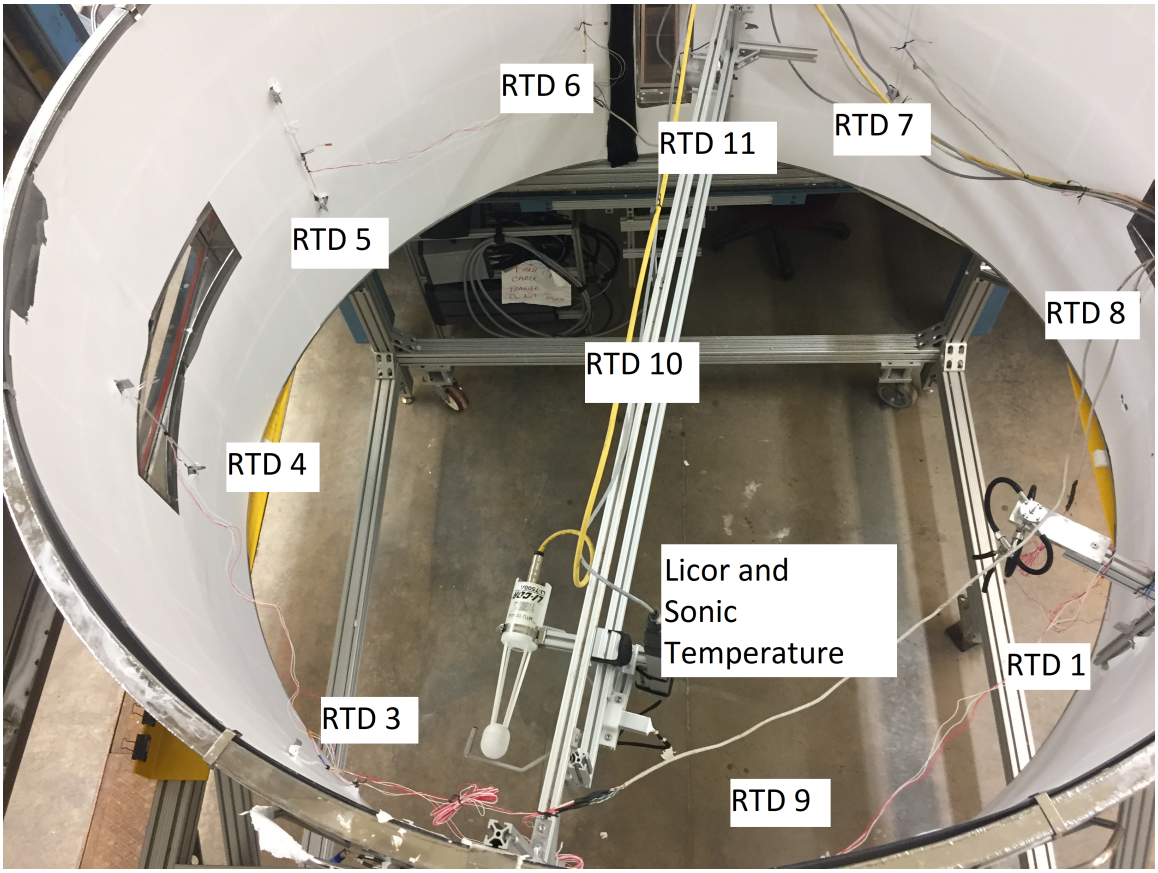

Figure 2.2: Photo showing the sensor locations (from above) for the moist convection experiments. The RTDs are 1 cm from the wall. The LiCor and sonic temperature sensor are collocated on the traverse that spans the chamber (see bottom of figure). RTD 10 is in the center of the chamber and is used for calibration of the sonic temperature. The diameter of the cylinder is 2 m.

As noted above, the primary measurement in Rayleigh-Bénard convection has been temperature, which can be measured with a variety of sensors with the required accuracy and precision. Quantitative measurement of concentration is much less common. Measurements of water vapor concentration are limited by the dynamic range of the sensor and temporal resolution (*e.g.* capacitance hygrometers) or by the path over which the measurement is averaged (*e.g.* absorption hygrometers). We use

a LiCor LI-7500A infrared hygrometer at 1 Hz to measure water vapor, with a 5 Hz averaging time. The path length, d, of the LiCor is 12.5 cm with a measurement volume of ≈ 12 cm^3. To ensure that we measure T with the same spatial and similar temporal resolution as r (to get a reliable value of S) we use a high speed sonic temperature sensor (Applied Technologies, Inc.); it has a path length of ≈ 13 cm and was set to sample at 1 Hz, with a 1 Hz averaging time. The sonic temperature sensor operates on the same physical principle as a sonic anemometer, using the transit time of an acoustic signal in order to calculate the speed of sound, which is a function of the temperature and humidity. In this case, the temperature sensor is sensitive to the virtual temperature, $T_v \simeq (1 + 0.61r)T$ [32], which can be converted to the actual temperature using measured water vapor concentrations from the LiCor. When the sonic temperature was near the center of the chamber, we calibrated the mean temperature derived from these two measurements against an RTD.

Both water vapor and temperature sensors were collocated on a traverse system so that they measured roughly the same volume. The traverse allowed us to move the sensors along a line that bisects the chamber. The three measurement points on traverse lie on a 5 cm offset from the line that bisects the chamber, with one near the center and two on opposing sides of the chamber. The two off-center locations will be referenced as the updraft and downdraft later in the paper and are about 20 cm from the nearest sidewall. The traverse system is located on the horizontal mid-plane ($z = 0.5$ m).When the sonic temperature was near the center of the chamber, we

calibrated the temperature derived from these two measurements against a nearby RTD. For the calibration, the mean temperature derived from the sonic temperature sensor and the LiCor was calculated when in the middle position of the traverse. That derived temperature was then adjusted to equal the mean temperature measured by RTD-10 in Fig. 2.1.

2.2.3 Experimental Strategy

In order to determine the behavior of the LSC we followed the method of Brown and Ahlers [22] and Xi et al. [13]. We use a ring of eight RTDs near the wall of the cylindrical chamber on the horizontal mid-plane of the chamber, and define the angular position (Θ) of the RTDs as the total angular distance (clockwise) away from an arbitrary position. The temperature measured by any of the eight RTDs is then

$$T(\Theta) = \overline{T} + \delta cos(\Theta - \phi) \tag{2.3}$$

where $\overline{T}$ is the mean temperature in the ring, δ is the amplitude of the temperature variation among the eight RTDs and ϕ is the phase of the temperature variation. δ and ϕ are derived by fitting the measurements to Eq.(2.3). Notably ϕ represents the angular location of the updraft relative to the reference position.

During dry convection we applied this procedure independently on two different sets

of eight RTDs, to characterize the behavior of the LSC and temperature distributions within the bulk. The placement of the two sets of RTDs formed an outer ring (Wall) and inner ring (Bulk) which were located 1 cm and 30 cm from the sidewall of the chamber.

We can describe the characteristics of the temperature in the chamber using only RTDs. If this were our only objective we would only need to run the chamber in dry conditions. However, in studying cloud properties we also need to describe the distribution of water vapor and by extension the saturation ratio. The traverse was introduced for the moist convection experiments in order to characterize the water vapor and saturation ratio at different locations in the flow. Due to physical limitations the center ring of RTDs cannot be used in tandem with the traverse.

Because our measurement of the water vapor mixing ratio is over a 12.5 cm path, we need to know how a volume/path averaged measurement will compare to an ideal (*i.e.* instantaneous, point) measurement. Because we cannot perform such a measurement for the water vapor concentration, we used a large-eddy simulation (LES) to understand the effects of path averaging on water vapor concentration and temperature.

2.2.4 LES results for path averaging

Our LES is the System for Atmospheric Modeling or SAM [78], which has been adapted and scaled to the conditions of our chamber. In Thomas et al. [79] the turbulent dynamics (energy dissipation rates, TKE and large scale oscillations) from the simulations have been matched with experimental values. The simulations reported here represent a 2×2×1 m cell with $\Gamma = 2$ (*i.e.* the chamber without the cylindrical insert in place) with adiabatic side walls. The LES grid is 64×64×32 with a spacing of 3.125 cm. The simulation was run with a time step of 0.02 s with a ΔT = 10 K and $\overline{T} = 10$ °C. We exclude the first 50 min of simulation time from our results. The analyzed portion of the LES results span 70 min of simulation time (30 and 42 times greater than the period of the LSC respectively). We placed 41 virtual temperature and water vapor sensors in the center of the cell. The sensors are arranged in four lines of 11, centered at (1,1,0.5) (all distances in meters). Fig. 2.3 shows the locations.

We use a single grid box as an 'ideal' measurement. We simulated the sensor's path length by averaging the temperature and water vapor of n adjacent points. We use the center bin as the reference and symmetrically average towards the ends of each line. The path length is then calculated by $d = n * 3.125$ cm along the x and y axes. On the diagonal the path length is calculated by $d = n * 3.125 * \sqrt{2}$ cm. The path length for a single point, denoted as d_0, is the size of a grid box, 3.125 cm.

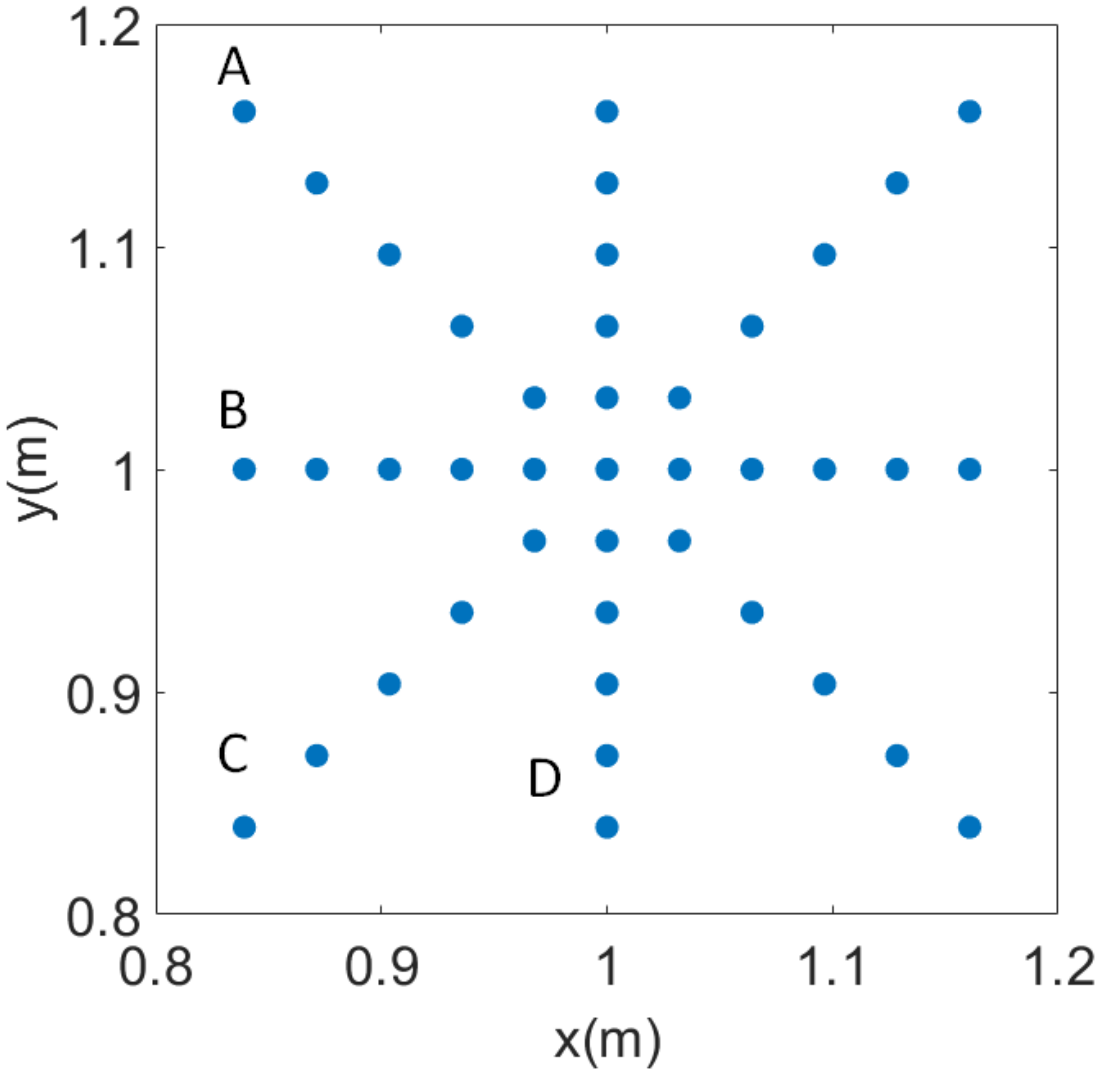

Figure 2.3: The positions of the virtual temperature sensors in the LES at $z = 0.5$ m.

The result of path averaging is shown in Fig. 2.4, which shows a plot of the standard deviation of temperature for a path length d, normalized by the standard deviation for d_0. Not surprisingly, as the path length increases, the normalized standard deviation of the measurement decreases. Also note that the curves from the four different lines

of numerical sensors collapse. (The lines are denoted A, B, C, and D in Fig. 2.4 and Fig. 2.5). Note that although only results for T are shown in Fig. 2.4, the data for $\sigma_r(d)\sigma_r^{-1}(d_0)$ and $\sigma_T(d)\sigma_T^{-1}(d_0)$ are identical due to the the non-dimensional units, and the same advective equations and diffusivity for both scalars. The LES results indicate that, over the path length of the LiCor and sonic temperature sensors, the standard deviations of T and r decrease by $\approx 8\%$. This result indicates that the measurements that we perform in the Π Chamber do not capture the true variability in the system, but capture over 90% of it.

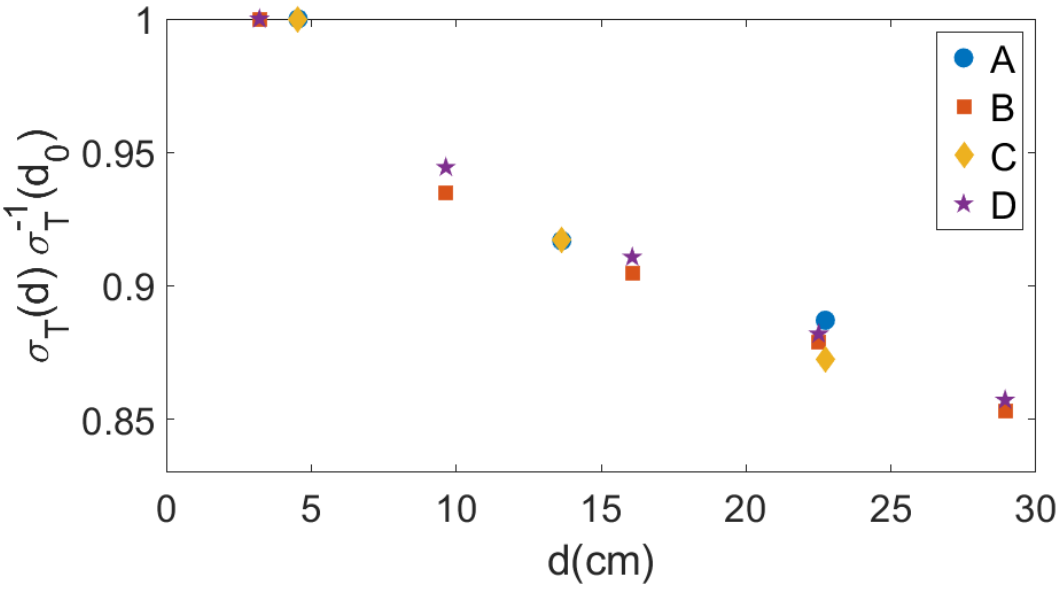

Figure 2.4: The normalized standard deviation of T as a function of the sensors path length. Path averaging over $\approx$ 12.5 cm results in a measured $\sigma(d)$ that is $\approx 92\%$ of $\sigma(d_0)$. See Fig. 2.3 for lines A, B, C and D.

The path averaged values for $r(d)$ and $T(d)$ were used with Eqn. 2.2 to calculate $S(d)$. In Fig. 2.5, $\sigma_S(d)\sigma_S^{-1}(d_0)$ is shown plotted against d. Over the same path

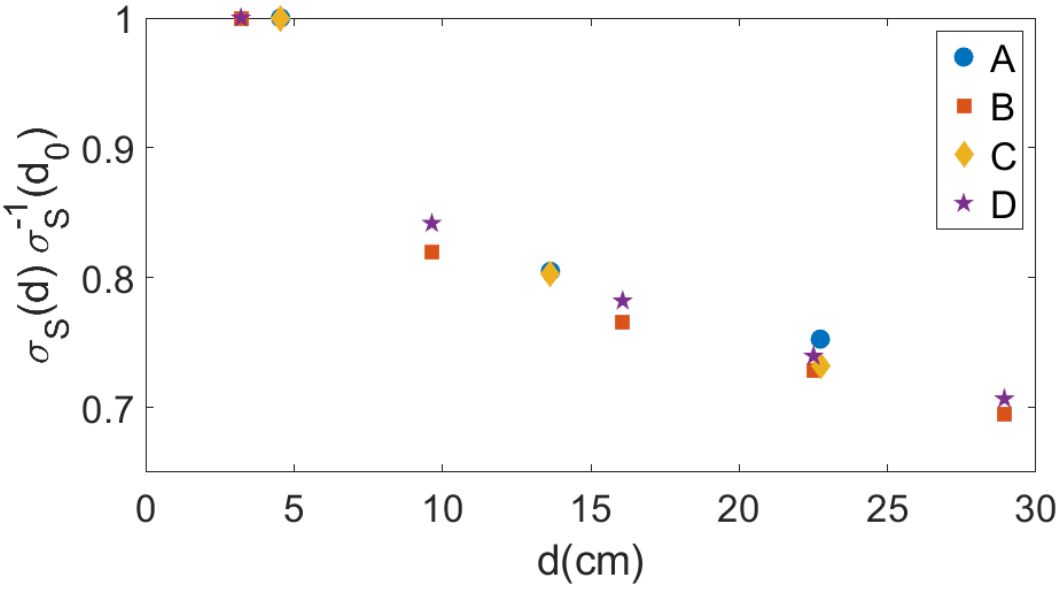

Figure 2.5: The path length averaged $\sigma_S(d)$ normalized by $\sigma_S(d_0)$ (the value measured in a single bin). Path averaging over $\approx$ 12.5 cm decreases σ_S to $\approx 81\%\sigma_S(d_0)$. See Fig. 2.3 for lines A, B, C and D.

length as the LiCor and sonic temperature sensors, σ_S decreases by $\approx$ 19%. The percent decrease in S over the path length of the LiCor is higher than 8% due to the combined averaging of r and T. We have shown that a path averaged measurement will underestimate the turbulent fluctuations. Path averaging is not the only type of averaging that is part of these measurement but we have determined that it is the most significant. For a further analysis of path averaging on the frequency spectra of T and the analysis of time averaging see *AppendixA*.

2.3 Determination of the basic characteristics of the LSC

We first ascertain the characteristics of the circulation, using only measurements of temperature (*i.e.* in dry conditions). For these conditions, we do not need to place the traverse with LiCor hygrometer and sonic temperature sensor in the chamber, so we can use the second ring of RTDs in the bulk of of the chamber (30 cm away from the side walls). In previous studies of Rayleigh-Bénard convection the first order moments of the circulation have been modeled as a single roll that spans the diameter of the cell using Eq. (2.3). This roll takes the form of a warm updraft along one side of the chamber with the cooler downdraft located along the opposite side. Due to the positive correlation between the vertical velocity and temperature, either variable can be used to find where the mean updraft is located [11]. The location of the updraft is then used to determine the orientation of the circulation.

An example of the instantaneous temperature measured on the wall and bulk rings is shown in Fig. 2.6. In the figure, the temperature fluctuation, $T' = T - \overline{T}$ is shown against Θ, where $\overline{T}$ is the mean temperature, averaged across all sensors in the ring and T is the temperature measured by a single sensor at time t. The solid line is the least squares fit to the temperature measurements using Eq. (2.3). In both rings

of RTDs, a sinusoid is a reasonable fit. The amplitude, δ, and the orientation, ϕ, were calculated from the fit; Fig. 2.7 shows the orientation of the circulation along the wall, $\phi_{Wall}(t)$, and in the bulk, $\phi_{Bulk}(t)$, as a time series. The difference between ϕ_{Wall} and ϕ_{Bulk} is smaller than the uncertainty in the fit. The uncertainty of the fit is ± 0.3 radians and ± 0.1 K for the orientation and the amplitude respectively. Over the course of our measurements the mean orientation for both precesses by ≈ 0.3 radians. Both rings of RTDs show azimuthal oscillations of ≈ 0.6 radians, which is inherent to the LSC [23]. The time series also shows that ϕ_{Wall} and ϕ_{Bulk} oscillate in phase.

In Fig. 2.8, the time series for δ_{Wall} and δ_{Bulk} are shown. The LSC does not show any cessations, with δ never approaching zero. The amplitude along the wall is consistently higher than the amplitude in the bulk. δ for both rings fluctuates around the mean by ≈ 0.1 C. The amplitude of the LSC being highest near the wall is consistent with the circulation predominately following the walls of the cell [80]. The strength of the LSC decreases towards the center.

As ΔT increases, the amplitude of the temperature on both rings increases, as shown in Fig. 2.9. For each ΔT, $\overline{\delta_{Wall}} > \overline{\delta_{Bulk}}$. As ΔT increases, the standard deviation of δ (σ_δ) also increases, showing that the variability of the LSC depends on ΔT. Over the range of ΔTs we have investigated, the amplitude for both rings increases linearly. In previous studies f_0 was shown to depend on ΔT [8, 24, 81] . Our periods we have

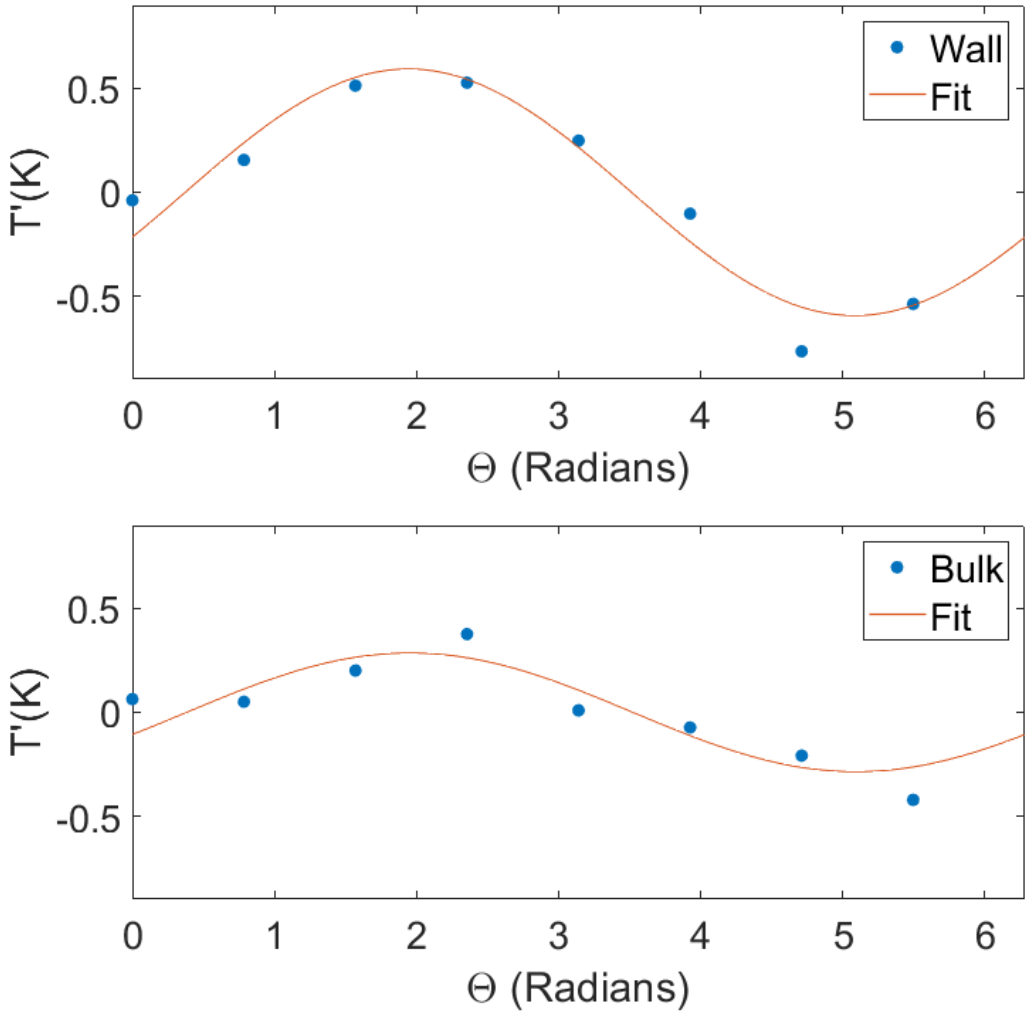

Figure 2.6: An example of the sinusoidal fit to the temperature fluctuations (T') with respect to the azimuthal position of the RTDs (Θ) along the wall (top) and in the bulk (bottom). The uncertainty in the temperature is too small to be seen on the graph. The goodness of the fit does not change over time

.

measured in this study are essentially the same as those in Niedermeier et al[8].

Our data show that the effects of the circulation are felt well into the bulk of the chamber, though, as expected, the amplitude of the circulation decreases towards

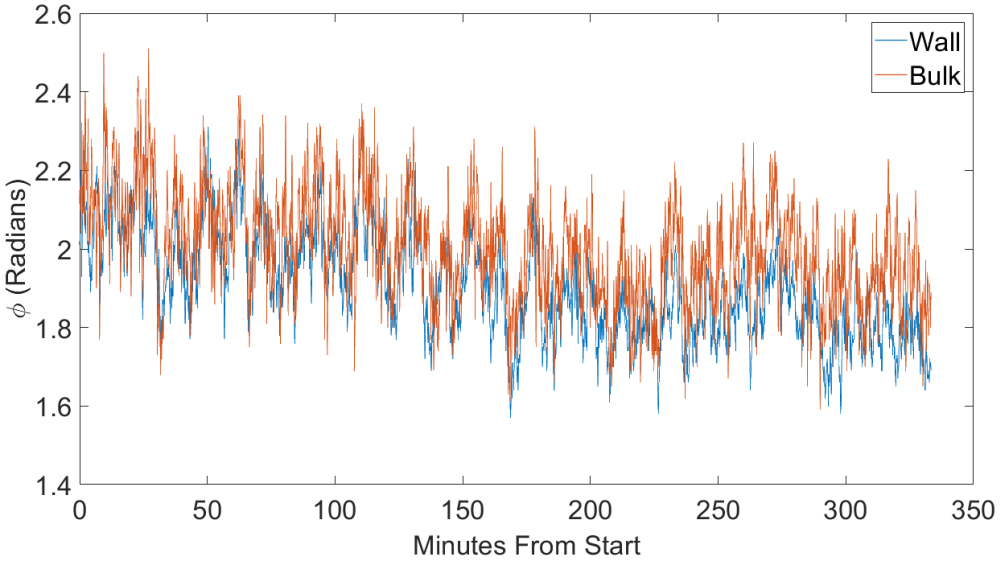

Figure 2.7: The azimuthal orientation (ϕ) of the Large-Scale circulation for a $\Delta T = 12$ K along the wall (red) and 30 cm towards the center (blue). ϕ is essentially the same for both rings of temperature sensors.

the center. Our results also indicate that the circulation in the Π Chamber has pronounced azimuthal oscillations about a preferred orientation. The preferred orientation is a result of asymmetries and the instrumentation in the chamber. We will now address the impact of the LSC on the temperature distributions in the bulk of the chamber, using the RTDs in the bulk ring.

To minimize the effect of the chamber's temperature controls, which can fluctuate on the order of ten minutes, a high-pass Fourier filter (ifilter with a center of 3.3145 and width of 0.82846) with a cutoff of around five minutes was applied to the individual RTDs in the inner ring. The cutoff at five minutes is roughly four times larger than the period of the large scale circulation ($1/f_0$), where f_0 is the large scale circulation

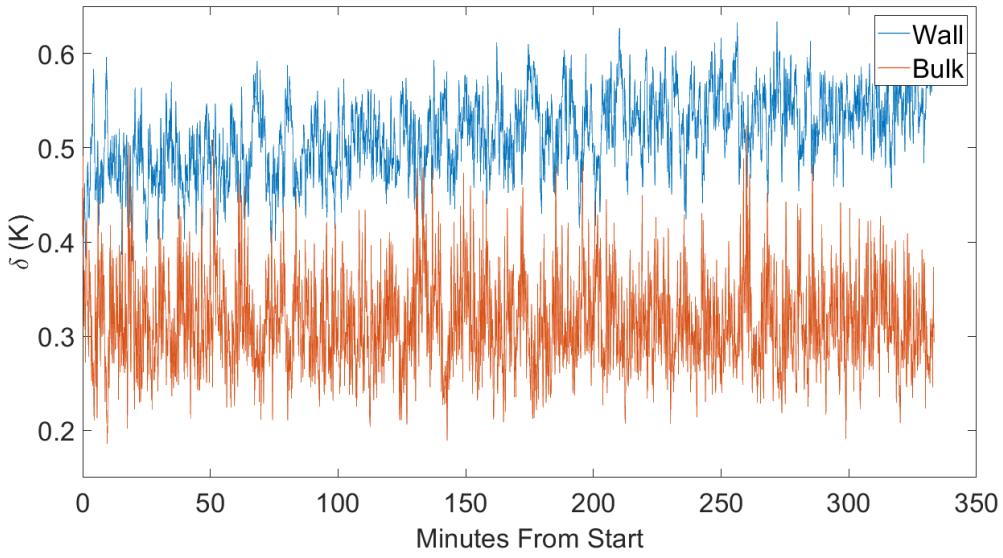

Figure 2.8: The amplitude (δ) of the Large-Scale circulation for a $\Delta T = 12$ K along the wall (red) and 30 cm towards the center (blue). The amplitude near the wall is consistently higher than in the bulk.

frequency. The angular deviation from the updraft was calculated from ϕ_{wall} using 16 bins of size $\pi/8$ radians to minimize the effect of azimuthal oscillations of the circulation. It should be noted that the azimuthal oscillations cause measurements from multiple RTDs contribute to the values calculated in each bin. With this done, the normalized standard deviation ($\sigma_T/\Delta T$) is shown in Fig. 2.10. Near the updraft ($\Theta - \phi_{wall} = 0$), $\sigma_T/\Delta T$ is lower than the rest of the chamber. The downdraft ($\Theta - \phi_{wall} = \pi$ and $\Theta - \phi_{wall} = -\pi$) curiously has a normalized standard deviation that is about twice the $\sigma_T/\Delta T$ in the updraft. In an ideal chamber σ_T is likely the same for both the updraft and downdraft. The Π-chamber has several factors (for example viewing windows) that cause $\sigma_T/\Delta T$ to deviate away from the ideal case.

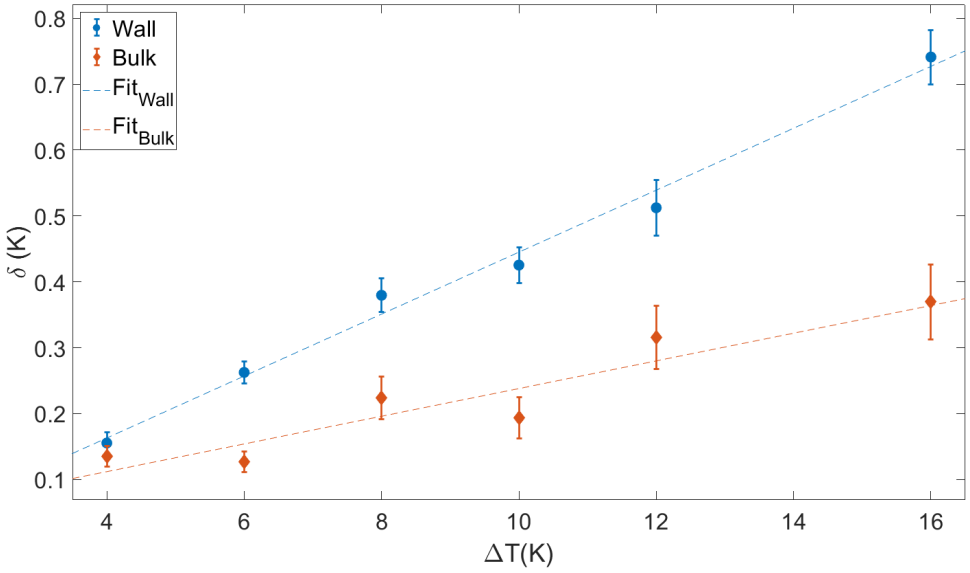

Figure 2.9: The amplitude, δ, of the Large-Scale circulation along the wall (red) and 30 cm towards the center (blue) for a range of ΔTs. The dashed lines are the linear fits to the wall(y=0.047ΔT-0.25) and the bulk(y=0.021ΔT+0.028). The uncertainties correspond to $\pm\sigma_\delta(\Delta T)$. At each ΔT, δ is higher along the wall than in the bulk.

In Fig. 2.11 the skewness of T is shown with the angular distance from the updraft of the LSC. The skewness is defined as $\mu_3 = \overline{(T-\overline{T})^3}/\sigma_T^3$. For each ΔT the highest skewness is measured when the temperature is near the updraft ($\mid \Theta - \phi_{wall} \mid = 0$) and lowest in the downdraft ($\mid \Theta - \phi_{wall} \mid = \pi$). Perpendicular to the axis of the circulation the distributions become symmetric. ΔT does not change the value of the skewness due to the normalization of the skewness. Multiple points in the same location are due to absolute value applied to $\Theta - \phi_{Wall}$. The same distance to the left and right of the circulation would then be expressed as two points at the same location away from the updraft.

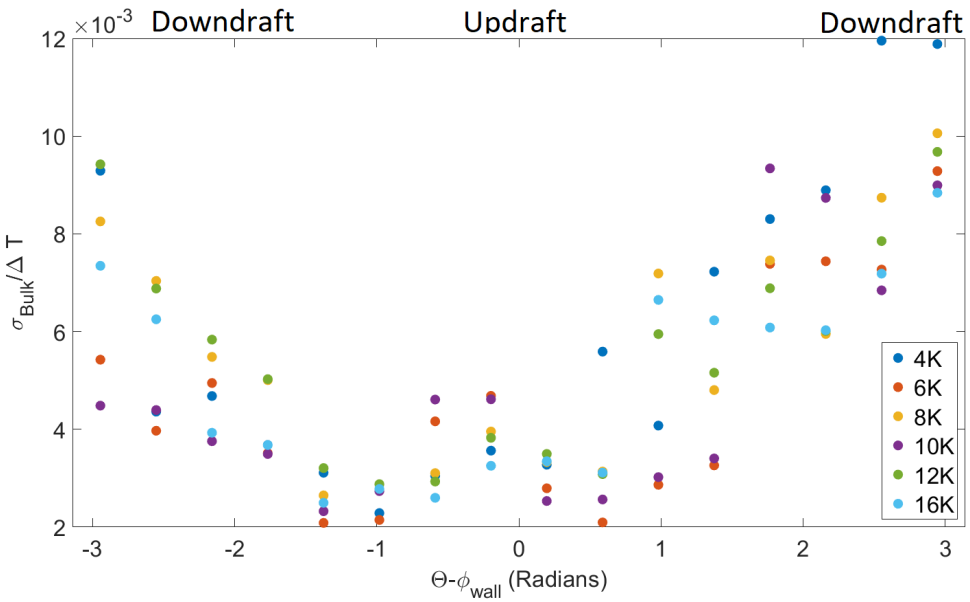

Figure 2.10: σ_T normalized by ΔT as a function of the angular displacement from the updraft. The temperature was filtered using a high pass Fourier filter with the cutoff at around 5 min.

The skewness is impacted greatly by rare events which likely contributes to the spread in values at each position from the updraft. In RBC rare events take the form of plumes that come from either the top or bottom boundaries. The positive skewness in the updraft is a result of warm plumes from the bottom surface. Alternately, cold plumes are more likely to pass through the downdraft, causing a negative skewness. Ideally in positions perpendicular to the LSC we expect warm and cold plumes to pass a sensor at an equal rate resulting in zero skewness. In Fig. 2.11, the spread of values perpendicular to the LSC ($\mid \Theta - \phi_{wall} \mid = \pi/2$) is likely due to the uncertainty in ϕ_{wall}. Within the uncertainty, the off-axis region could be slightly closer to the updraft or downdraft. For example at $\Theta - \phi_{wall} = \pi/2$ warm plumes could be more frequent than cold plumes, despite being calculated at a spot were they should have equal

probability. Directly across from those sensors ($\Theta - \phi_{wall} = -\pi/2$), the cold plumes may be more frequent than warm plumes. Both measurements would be represented at $\mid \Theta - \phi_{wall} \mid = \pi/2$ but the skewness would have the opposite sign.

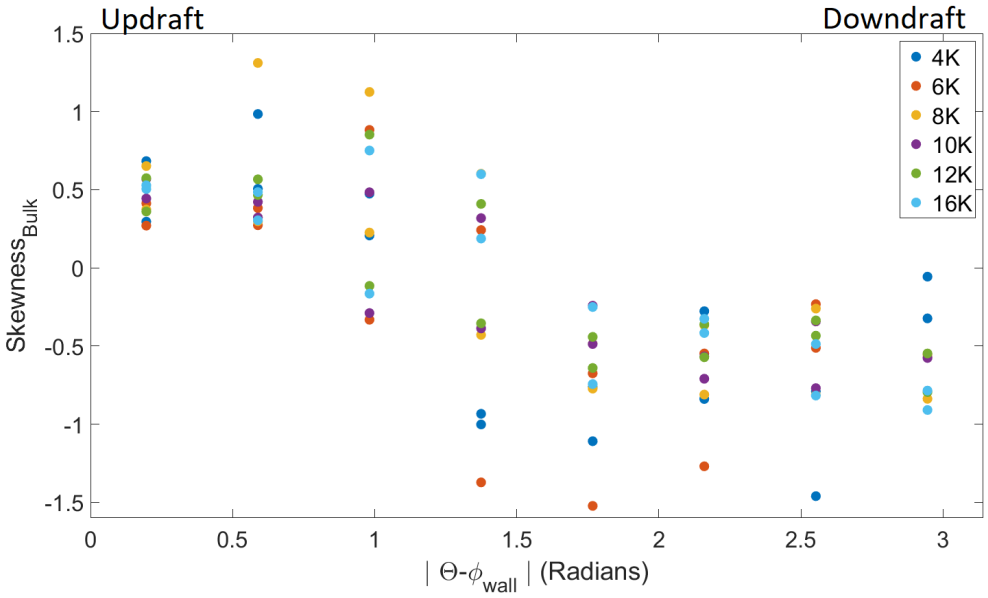

Figure 2.11: The skewness of the temperature measurements as a function of the angular distance from the updraft. The temperature was filtered using a high pass Fourier filter with the cut off at around 5 min. Near the updraft the temperature fluctuations are positively skewed. Near the downdraft the temperature fluctuations are negatively skewed. ΔT does not change the value of the skewness.

2.4 Moist convection results

Having established the basic characteristics of the large scale circulation, using measurements of the temperature, we turn to the scenario in which a difference in temperature and water vapor concentration between the top and bottom plates drives a

convective flux of two scalars. The Rayleigh number is dominated by the temperature difference; the difference in water vapor concentration is small in comparison, which follows from Eq. (2.1). Given that, the behavior of the temperature field in the bulk of the chamber will be comparable in moist and dry conditions.

As noted in Sec 2.2, the inner ring of RTDs was removed to enable measurement of temperature and water vapor with the sonic temperature sensor and LiCor respectively. These instruments were mounted such that they were probing roughly the same volume; additionally the sensors were mounted such that they could be moved across the chamber on a traverse. The time series of r, T and S are shown in Fig. 2.12 for $\Delta T = 12$ K. The sensors were near the updraft and downdraft for 4 hrs each. The sensors were in the center for 8 hrs. The figure clearly shows that the variance of the scalars is a function of the position in the large scale circulation. Near the downdraft of the circulation, the variance is the highest. This is consistent with the standard deviations near the downdraft shown in Fig. 2.10.

A Fourier analysis of r and T in the center of the chamber are shown on the right side of Fig. 2.12. The main peak is at a period of ≈ 72 seconds which is due to the large scale circulation frequency, f_0, which has been shown to be caused by the azimuthal oscillations of the LSC [13]. Harmonics of f_0 can be seen in both measurements. For a more detailed analysis of Fourier spectra in the chamber, see Niedermeier et al [8].

As another perspective on these measurements, we show the probability distribution

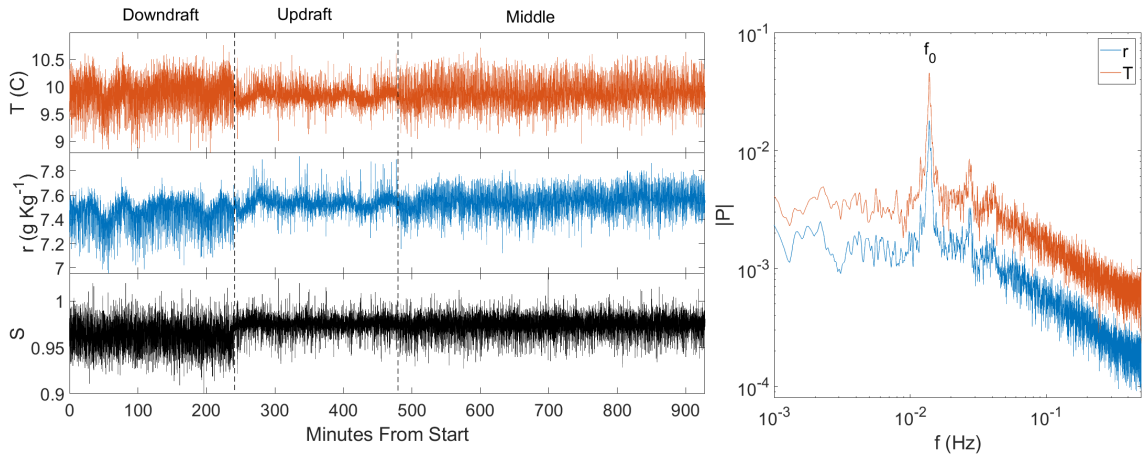

Figure 2.12: The left panel shows the time series of temperature (T, red), water vapor mixing ratio (r, blue) and the saturation ratio (S, black) at different positions in the Π-chamber. The time series only include periods in time where the chamber is in steady state conditions. At the beginning of the time series the traverse was near the downdraft side of the chamber. At 240 minutes from the start the sensors were moved to near the updraft. At 480 minutes they were moved to the center of the chamber and remained there until the end. The right panel contains the Fourier spectrum of r and T while the sensors are in the center of the chamber. The oscillation frequency, f_0, corresponds to a period of ≈ 72 seconds. The spectra are smoothed for clarity.

functions (PDFs) for T' in the top of Fig. 2.13. (It should be noted the fluctuations in the top and middle of Fig. 2.13 are in relation to the temporal average at each individual measurement position along the traverse.) The standard deviations and skewness of T, r and S are presented in Table 2.1. The standard deviations of T in the moist case are consistent with the trends seen in Figs 2.10 and 2.12 where the downdraft of the circulation has the highest variance. The skewness for T is positive near the updraft, and negative near the downdraft. These values for the skewness are consistent with the values calculated from the RTDs in Fig 2.11. The middle of Fig. 2.13 shows the PDF of r'; the overall shape of the distributions is similar to

the distributions of T'. Like σ_T, σ_r is lowest near the updraft and highest near the downdraft. The skewness for r follows the same trend as T with a positive skewness near the updraft and a negative skewness near the downdraft. Taken together, the distributions of T' and r' reinforce the phenomenological picture that warm, humid plumes are more likely to be seen in the updraft region of the chamber. The opposite is true for the downdraft, where the presence of cold, low r plumes lead to both distributions being negatively skewed.

In the bottom of Fig. 2.13 is a plot of the probability distributions of $S - \overline{S}_{middle}$. We have subtracted the mean of the saturation ratio from the middle of the chamber to highlight the fact that the downdraft has a lower mean than does the updraft or core region of the chamber. The distributions of $S - \overline{S}_{middle}$ are quite similar in the updraft and in the middle of the chamber, while the distribution in the downdraft is broader (see Table 2.1).

Because of the correlation between temperature and water vapor concentration in the chamber, a change in either r or T will not *a priori* lead to a change in S. A positive fluctuation in T could be associated with a positive fluctuation in r such that the ratio of r and r_s do not change. (See Chandrakar et al.[76] for a more complete discussion of the correlation between r and T and the corresponding changes in S.) Our data show that the skewness of r and T are comparable in both sign and magnitude in the updraft region of the circulation. S however, is negatively skewed at each location in

Position	$\overline{T}$(C)	σ_T(K)	$skewness_T$	$\overline{r}$(g/kg)	σ_r(g/kg)	$skewness_r$	$\overline{S}$	σ_S (%)	$skewness_S$
Updraft	9.83	0.12	0.50	7.53	0.05	0.50	0.97	0.69	-0.50
Middle	9.88	0.19	0.26	7.55	0.08	-0.21	0.97	0.82	-0.64
Downdraft	9.89	0.22	-0.52	7.45	0.09	-1.08	0.96	1.19	-0.18

Table 2.1

The statistics for r, T, and S at each position along the traverse during moist conditions and ΔT=12K.

the chamber.

2.5 Conclusions

The convection-cloud chamber at Michigan Tech, the Π Chamber, is a Rayleigh-Bénard convection cell, designed for studies of interactions between turbulence and cloud microphysics. Through measurements of the temperature in the chamber, we have shown that the large scale circulation is a single roll with a fixed overall orientation, but with pronounced oscillations about the mean position, typical of the large scale circulation in Rayleigh-Bénard convection.

To determine the saturation ratio in the chamber, we measure water vapor concentration and temperature, simultaneously, to get the saturation ratio, S. Because point measurements of water vapor concentration are not currently possible, we have verified that our path averaged measurements capture an acceptable fraction of the true variance in the system, using a combination of measurements and large eddy simulations. The LES shows that σ_T and σ_r decrease by $\approx 8\%$ from their true values when the measurement is averaged over approximately 12 cm, as ours are. The corresponding decrease in S is $\approx 19\%$. (Path averaging is more pronounced for σ_S due to the combined averaging from r and T.) The LES shows that path averaged measurements do underestimate but still represent a sizable portion of the turbulent

fluctuations of r, T, and S.

We show that water vapor concentration and temperature distributions in the updraft and downdraft are qualitatively similar. For example, both scalars in the updraft are positively skewed and have a higher mean than the center. Combining these measurements into S shows turbulent fluctuations that are caused by fluctuations in r and T. S is consistently negatively skewed even in the updraft where both r and T are positively skewed. In the downdraft the distribution of S is more negatively skewed than the updraft. While our results show significant fluctuations in r, T and S, the true variability on scales felt by cloud droplets would likely be higher than what we have reported because of the path lengths of our sensors.

As noted in the Introduction, one of the primary motivations to understand the spatial and temporal variability of the saturation ratio in the chamber is to then relate it cloud droplet growth. In previous analyses of microphysics in the chamber, zero and first order models of the variability in the saturation ratio have been used [51, 76]. The results presented here indicate that while these models capture the essential variability (standard deviations) of T, r, and S in the center of the chamber, spatial variations of the mean in the chamber may affect, for example, where droplets preferentially activate or evaporate. How these spatial differences impact cloud droplet distributions and how cloud droplets alter the saturation field are ongoing topics for both experimental and modeling efforts.

Future work will focus on how the fluctuations of S change upon the transition from moist to cloudy conditions. The in-cloud saturation field is dependent on the initial S (the moist conditions that we have shown in this paper) and the influence of cloud droplets. The presence of droplets is expected to buffer the fluctuations in S, but the magnitude is currently unknown.

2.6 Appendix A

We have shown that a path averaged measurement will underestimate the turbulent fluctuations. This type of averaging likely acts as a low pass filter, with the high frequency fluctuations being removed. In Fig. 2.14 the power spectra of T are shown for several different path lengths. As the path length is increased, the higher frequencies are proportionally removed at a faster rate, decreasing the slope of the spectra. Over the path length of the LiCor (≈ 12.5 cm) the spectra are noticeably impacted by the path averaging, but represent the overall shape and magnitude of the spectra of temperature reported by the single bin.

Not only does the path length of a sensor artificially dampen scalar fluctuations, but the sensor's time averaging must have a similar affect. For temperature, one cause of time averaging is the sensor's thermal mass. Ideally a thermometer would have a small mass, allowing it to rapidly respond to changes in temperature. This is one

of the reasons that we have used both rtds (which have a non-negligible thermal mass) and the sonic temperature sensor, which does not. The other cause is digital averaging over multiple samples from the same sensor. In our case, the high speed temperature system digitally averages over one second to output data at 1 Hz. This section will discuss the impact of digital time averaging on the fluctuations of T and S.

To estimate the effect, we took the output of the virtual sensor of the LES in each of the four corners and the center (see Fig. 2.3). The averaging time ($t*$) was simulated by applying a moving average of varying size to the LES output. In Fig. 2.15 the standard deviation was then calculated for the averaged time series and normalized by the standard deviation of the original time series ($\sigma_T(t_0)$). Over the averaging time of the sonic temperature sensor (one second), the standard deviation decreases to $\approx$ 94% $\sigma_T(t_0)$. This percentage is slightly higher but still comparable to the 12.5 cm path averaged measurement.

In Fig. 2.16 the time averaging for S was calculated using the time averaged values of both r and T. When the value was averaged over 1 second, the fluctuations in S decrease to $\approx$87% of the ideal value. Notably, the decrease in fluctuations of S for the path averaged measurements showed a decrease to $\approx$81% $\sigma_S(t_0)$. Clearly time averaging of the sensors should not be ignored; however in our case the path averaging of the sensors is the main contributor to suppression of fluctuations.

2.7 Acknowledgments

We thank the US National Science Foundation (AGS-1754244) and the US Department of Energy (DE-SC18931) for funding. Superior, a high-performance computing infrastructure at Michigan Technological University, was used in obtaining results presented in this publication.

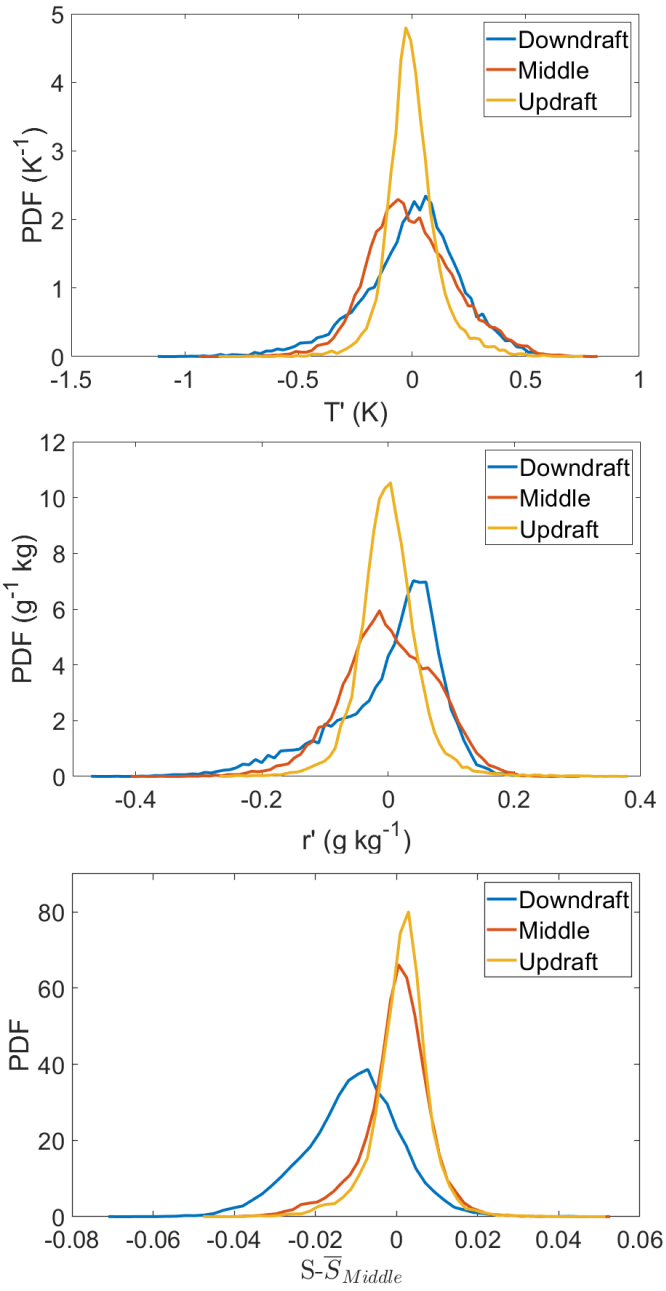

Figure 2.13: The probability distributions of T'(top), r'(middle), and $S - \overline{S}_{middle}$ (bottom) near the updraft, downdraft and middle. For each region a high pass filter was applied to r and T with a cut off of ≈ 5 min, to remove low frequency oscillations due to the slight drift in the chamber controls. We have plotted the distributions $S - \overline{S}_{middle}$, not S' to highlight the fact that the downdraft has a lower mean relative the middle and updraft.

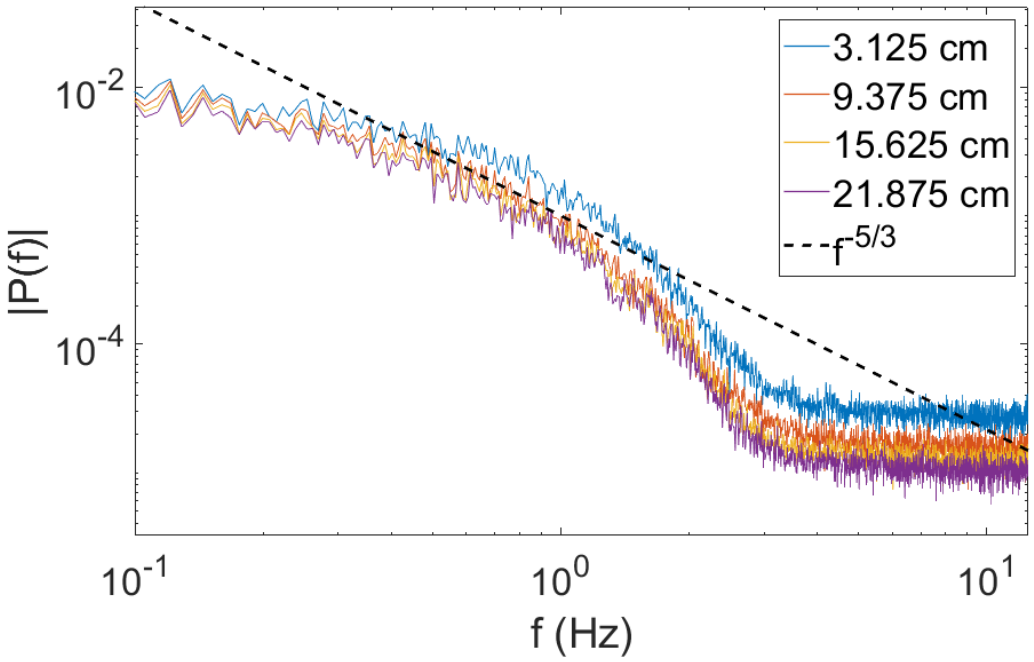

Figure 2.14: The spectra of the temperature measurement for several different path lengths. These spectra are averaged along line B and are smoothed for clarity. The dashed line is a power law ($f^{-5/3}$) included as a reference.

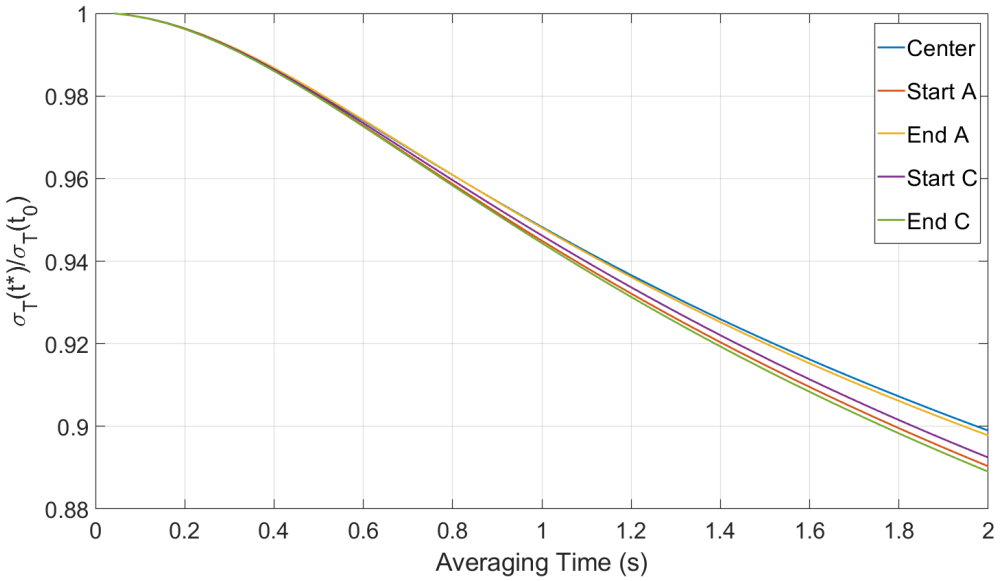

Figure 2.15: The time averaged $\sigma_T(t*)$ normalized by $\sigma_T(t_0)$ (the standard deviation of the raw temperature time series). Over the time averaging of the sonic temperature sensor, σ_T decreases to ≈94% $\sigma_T(t_0)$.

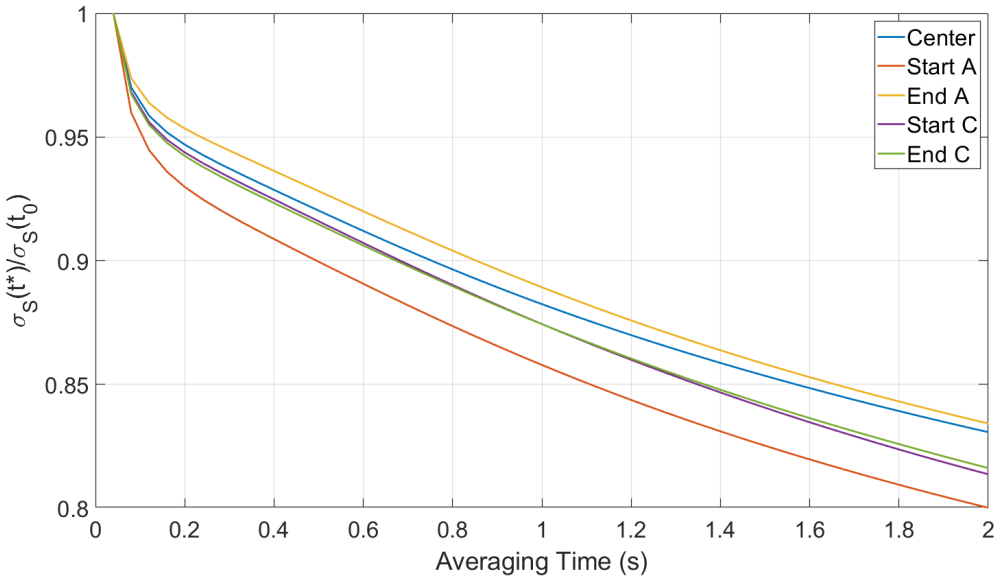

Figure 2.16: The time averaged $\sigma_S(t*)$ normalized by $\sigma_S(t_0)$ (the standard deviation of the raw saturation ratio time series). Over the time averaging of the sonic temperature sensor, σ_S decreases to ≈87% $\sigma_S(t_0)$.

Chapter 3

Turbulent Fluctuations of the In-Cloud Saturation Ratio

This chapter details measurements of the saturation ratio in a warm cloud, generated in the Π chamber. This work is in preparation for publication [1].

3.1 Introduction

The concentration of water vapor in air is one of the most basic quantities in atmospheric science. Indeed, students in the discipline learn its various definitions almost

[1] Anderson, J. C., Helman, I., Shaw, R. A., & Cantrell, W. Turbulent Fluctuations of the In-Cloud Saturation Ratio. To be submitted.

immediately, which is not surprising, considering the fact that both the mean and fluctuations about that mean on a variety of time scales play key roles in determining Earth's weather and climate. As just two examples, the average concentration of water vapor determines its impact as a greenhouse gas while fluctuations about the mean are important when considering phenomena like propagation of electromagnetic radiation in the visible portion of the spectrum through the atmosphere [82, 83]. Both the mean and fluctuations can be important when considering the growth of cloud droplets [33, 84, 85, 86, 87, 88]. Clearly, information on both mean and fluctuations are needed to understand the impact of water vapor in the atmosphere.

The water vapor mixing ratio is defined as $r \equiv \frac{m_v}{m_a}$, where m_v is the mass of water vapor in a volume of air and m_a is the mass of dry air. Because three phases of water (gas, liquid, solid) coexist in the atmosphere, a second measure of water vapor abundance is also commonly used, the relative humidity or saturation ratio:

$$S_{liquid} \equiv \frac{e}{e_s} = \frac{r}{r_s(T)} \tag{3.1}$$

where e is the partial pressure of water vapor. The subscript s denotes a value taken in equilibrium with a plane surface of pure, liquid water at the temperature T. The temperature dependence of the saturation vapor mixing ratio, r_s, is explicitly noted in the final term of Equation 3.1. S is a measure of how close the ambient water vapor concentration is to the concentration required for equilibrium with liquid

water. Values of S above or below 1 can be interpreted as the thermodynamic forcing toward condensation or evaporation [32, pg. 174].

Growth of a single cloud droplet from vapor is typically written in a form similar to Equation 3.2 [32, pg. 328]:

$$\frac{dm_d}{dt} = 4\pi r_d \rho_l G \left(S - S_K\right) \tag{3.2}$$

where m_d and r_d are the mass and radius of the drop, respectively, ρ_l is the density of liquid water, S_K is the saturation ratio at the surface of the droplet, and G incorporates surface and heat transfer effects. The appearance of the saturation ratio in this expression is a bit surprising when considered in the context of the development of the expression for droplet growth. The driving force for condensation (or evaporation) is the difference in the water vapor concentrations at the surface of the droplet and at infinity [32, pg. 324]. However, the historical development has been to replace that difference in water vapor concentrations with a difference in saturation ratios, which is what we adopt here.

While Equation 3.2 is straightforward for a single cloud droplet, it is usually applied to ensembles of droplets as well, which presents some difficulties. As a number of authors have noted [33, 84, 85, 86], S, on the right hand side of Equation 3.2, is ambiguous. The saturation ratio is almost certainly not uniform over a given volume

of air. If aerosol particles are clustered, competition for vapor may deplete the local concentration of water vapor and thus S [84, 85]. Growing water drops release latent heat to the surroundings, increasing the local temperature, also reducing S [86]. In addition to effects from the presence of multiple droplets within the volume, clouds are ubiquitously turbulent, which induces fluctuations in the concentrations of scalars such as water vapor and temperature [33, 76]. In short, there is no single value for S, as it varies as a function of spatial position and time due to a combination of effects.

High speed measurements of S are challenging in a saturated or supersaturated region. In fact, a majority of humidity sensors commonly used can only be used when the relative humidity is below 100%, unless the sensor is heated [89]. As a result, measurements of S in a cloudy environment are rare. In 1991, Gerber et al. showed the saturation ratio in fog fluctuates due to mixing [56]. Aircraft measurements made by Ditas et al. and Siebert and Shaw included high speed measurements showing the in-cloud spatial variability of S [57, 58]. Laboratory measurements of S in a supersaturated environment were made by Anderson et al. [90] in the MTU Π chamber. However these measurements were performed in the absence of cloud droplets.

Our aim here is to quantify the variation in S and its effects on an ensemble of cloud droplets in a laboratory facility, the Π Chamber [68]. We measure both the water vapor density and temperature in turbulent environments with varying concentrations of aerosol particles and cloud droplets. With this data set, we quantify an intrinsic

variation in S under cloudy conditions, which contributes to understanding processes in the atmosphere, such as growth of cloud droplets, which are affected by that variability.

3.2 Methods

Measurements were made in the Π chamber, described in detail in Chang et al [68]. Here, we provide only a brief overview. The chamber is a turbulent Rayleigh-Bénard convection (RBC) cell in which the lower surface of the chamber is set to a higher temperature than the upper. These conditions induce turbulent mixing due to the buoyancy difference between warm and cool air. As the air mixes it results in fluctuations in the temperature and water vapor concentration. For the typical conditions we employ, the Rayleigh number in the chamber is $\sim 10^9$.

For all of the experiments reported here, the temperature difference in the chamber was 16 K. The mean temperature was 20 °C, with T_{side} = 20 °C, T_{top} = 12 °C, and T_{bottom} = 28 °C. The surfaces of the chamber are wetted, such that the convection transports both heat and water vapor. We use moist and cloudy conditions in the chamber, the difference being that in moist conditions, the chamber is supersaturated, but there is no cloud formation due to lack of cloud condensation nuclei. In cloudy conditions, we inject size selected sodium chloride (NaCl) aerosols of diameter 130 nm

into the chamber using a differential mobility analyzer (DMA, TSI model 3071). (Note that because of multiple charging effects, there is also a mode of particles with diameter of approximately 200 nm injected, but the magnitude of this mode is much smaller than the one at 130nm.) By varying the number concentration of particles injected into the chamber, we can achieve droplet concentrations ranging from 10s to 100s cm^{-3}. Note that the concentrations stated in this paper refer to the concentration of aerosol in the air stream injected into the chamber. For example, injecting 3.14×10^3 particles cm^{-3} at 2 lpm into the chamber would correspond to an addition of 2 particles cm^{-3} min^{-1} of the chamber volume.

We measured the water vapor mixing ratio, r, using a LiCor LI-7500A infrared hygrometer. It has a path length of $\approx$ 12.5 cm, and has an averaging time of 0.2 seconds. In order to best match the path length and temporal averaging of the water vapor measurement, we used a high speed sonic temperature sensor (Applied Technologies Inc.) to measure temperature, T. The sonic temperature sensor was set to sample at 1 Hz and has a path length of $\approx$13 cm. The mean value of the sonic temperature sensor was calibrated to a co-located 100 Ω thin film, platinum resistance thermometer (RTD, Minco, S17624, $100\Omega \pm 0.12\%$). The LiCor and the sonic high speed temperature sensor are placed near the center of the chamber. The sensors path lengths were parallel to each other and separated by $\approx$ 3 cm.

Both the path length and temporal averaging of the sensors can artificially suppress

measured fluctuations in r, T, and subsequently, the saturation ratio, S. In our case, the path averaging has a larger effect on S than temporal averaging. Despite this averaging, our setup still captures a large portion ($\approx$ 81%) of the turbulent fluctuations. These issues are discussed in more comprehensive detail in Anderson et al. [90].

We use the measured values of r and T to calculate the saturation ratio S, defined in Equation 2.2. In practice, the saturation values ($r(T)_{sat}$) in the equation are calculated from the Clausius-Clapeyron equation, using the measured value of T [32]. Measurements from subsaturated conditions ($S < 1$) are discussed in Anderson et al.[90]. Here we focus on differences between moist and cloudy conditions.

We also use r and T to calculate the moist static energy, MSE, defined as

$$MSE \equiv c_p T + l_v r \tag{3.3}$$

where c_p is the heat capacity of the air mass and l_v is the latent heat of condensation. (Note that for our case, we have dropped the geopotential, Φ, from the definition of moist static energy since it is essentially constant over the volume of the chamber.) The moist static energy is unchanged by condensation as energy is simply shuffled between the two terms on the right hand side of Equation 3.3.

In cloudy conditions, the injected aerosol activate and grow to the size of cloud droplets. Values of the liquid water content and the mean droplet diameter were derived from measurements made with the WELAS 2000 Digital optical particle counter, which is sensitive to size ranges of 0.6 to 40 μm in diameter. The size distributions were averaged over 100 s at a flow rate of 5 lpm.

3.3 Results

Time series of r, T, S, and MSE for a moist to cloudy transition are shown in Fig. 3.1. The blue line in the figure shows the measured or calculated values while the red line is a 5 minute running mean. (Note that the data has been filtered to remove oscillations associated with the chamber controls, which are on the order of 10 minutes. See discussion in Anderson et al.[90] for details.) The experiment begins by letting the chamber come to a dynamic equilibrium in the moist state. For the first 4000 seconds, the mean values of all four variables shown in the figure are roughly constant, with significant excursions above and below the mean, consistent with the fully developed turbulence in the chamber.

At $\approx$ 4000 seconds, NaCl aerosols are injected into the chamber, forming a cloud, marked by the first vertical black line in all four panels of the figure. Shortly after aerosol injection, there is a decrease in r and a corresponding increase in T from the

latent heat of condensation. As expected, S decreases due to the combined changes of r and T as water vapor condenses to liquid. Also as expected, the moist static energy is unchanged from moist to cloudy conditions. Upon cloud formation, the system begins to relax to a new dynamic equilibrium, as cloud condensation nuclei (the NaCl aerosol) activate, grow as cloud droplets, and settle out of the chamber. (Note that the activation, growth, and removal need not be monotonic in all conditions [91].) The length of the transition period was roughly 45 min, which is determined when $\overline{S}$ is constant and the droplet size distributions of two successive measurements agree. The time required to achieve the new steady state changes depending upon the injection rate. The second black, vertical line in the panels of the figure mark the end of the transient response and establishment of steady state. The end of the transient is not as clearly defined as is the onset of cloud formation.

Fig. 3.2 is another perspective on the moist to cloudy transition shown in Fig. 3.1. Upon introduction of CCN to the chamber, the probability density function (PDF) of r shifts to lower values, consistent with water vapor being removed from the volume as it condenses to cloud droplets. Similarly, the PDF of T shifts to higher values as the air in the volume is warmed by the release of latent heat. Combining the two effects, the saturation ratio is reduced, as expected. The moist static energy is essentially unchanged. For the cases shown here, the transition from moist to cloudy conditions does not dramatically change the variance of r, T and MSE. In this instance, there is a slight decrease in the variance of S, although such a decrease is not seen in every

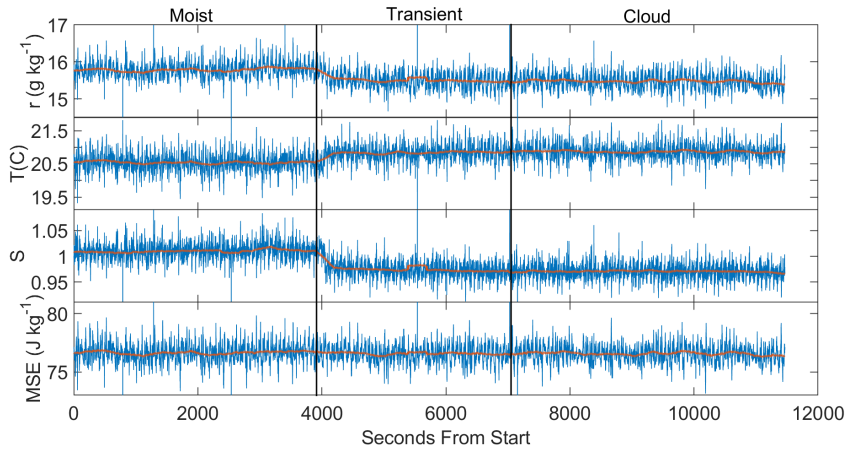

Figure 3.1: The time series of water vapor mixing ratio, temperature, saturation ratio and moist static energy for one of the experiments, showing the moist to cloudy transition. Cloud formation is initiated at $\approx$ 4000 seconds with the injection of 130 nm diameter NaCl aerosol with a concentration of 145,000 $\pm$ 5000 cm^{-3}. The left vertical black line marks the onset of aerosol injection. The second vertical black line marks the end of the transient response and the beginning of the stead-state cloudy conditions. Close examination of the figure reveals a periodicity in all of the quantities presented here, which is a signature of oscillations in the large scale circulation in the chamber [90].

experiment that we conducted.

Fig. 3.3 is a plot of the water vapor mixing ratio as a function of temperature for the moist (top panel) and cloudy (bottom panel) conditions shown in Fig. 3.1. The saturation mixing ratio is shown as the solid line in the figure, while the dashed line shows the mixing ratio expected if the only process in the chamber were mixing of plumes from the top and bottom saturated surfaces. (See Shawon et al. [92] for further discussion of these boundary conditions.) The red circles are averages of r in 0.01 °C increments.

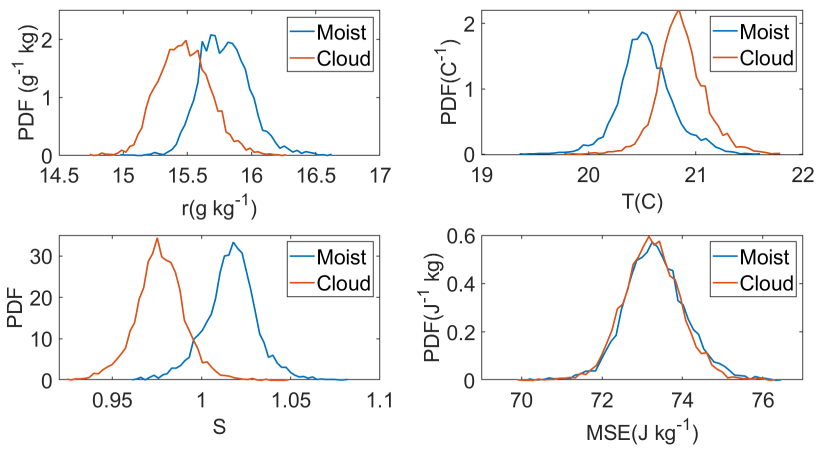

Figure 3.2: PDFs for moist (blue line) and cloudy (red line) conditions for r, T, S and MSE for the time series shown in Fig. 3.1. The shifts in r, T, and S and the lack of a shift in MSE are consistent with water vapor condensing onto the injected aerosol to form a cloud.

Consistent with Figs. 3.1 and 3.2, the data are concentrated around a temperature of 20.5 °C and approximately 15.75 g kg^{-1} in moist (*i.e.* before cloud formation) conditions. The mean values shift to a slightly higher temperature and lower water vapor concentration upon injection of CCN, consistent with the results already discussed. The mean water vapor concentration in each temperature range (red circles) also shifts to lower values, though the slope of a fit line through those points (not shown) does not change appreciably upon cloud formation. One striking feature evident in Fig. 3.3 is the range of vapor mixing ratios for a given temperature. At 20.5 °C, there is a 1 g kg^{-1} spread in vapor mixing ratios, which is roughly consistent across the range of temperatures measured.

As noted above, the data shown to this point have been for a moist to cloudy transition upon injection of approximately 145,000 particles cm^{-3} at 2 lpm into the chamber.

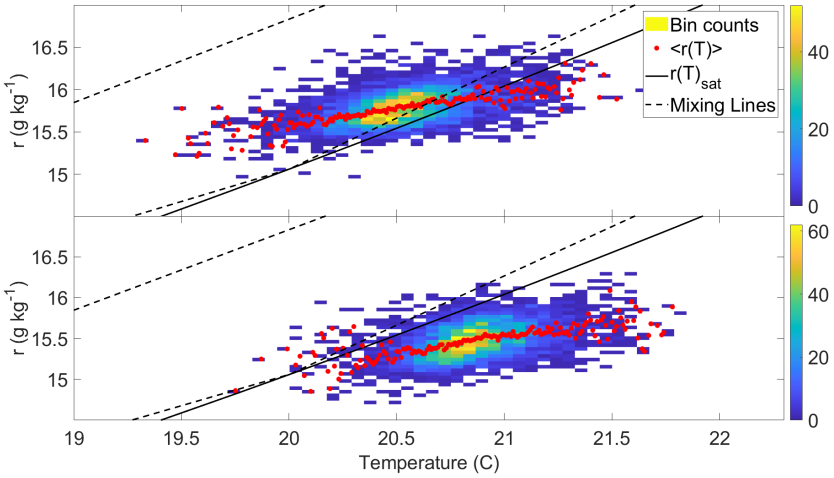

Figure 3.3: Water vapor mixing ratio as a function of temperature for moist (top panel) and cloudy (bottom panel) conditions. The data shown here corresponds to the time series shown in Fig. 3.1. The density of measured points (*i.e.* data acquired at 1 Hz) is shown in the color scale to the right of the plot. The red circles were calculated by averaging $r(T)$ in a temperature bin of width 0.01 K. The solid black line is the saturation mixing ratio as a function of T (*i.e.* the Clausius-Clapeyron line) while the dashed black lines show the water vapor mixing ratio expected if the only process in the chamber were mixing of plumes of air from the side, bottom, and top surfaces.

We also conducted experiments in which the injection was approximately 10^4, 5×10^4, 10^5, and 2×10^5 particles cm^{-3}. The results are qualitatively similar over seven different experiments. (We repeated selected experiments, which is why experiments outnumber conditions.) We turn to a discussion of differences among these experiments by first establishing the baseline. The top panel of Fig. 3.4 is a plot of the PDFs of the saturation ratio, S, for all seven experiments for the time period approximately one hour before aerosol injection. The distributions for each day are in agreement, with the exception of a slightly drier chamber on August 27, showing our initial conditions before cloud formation are consistent.

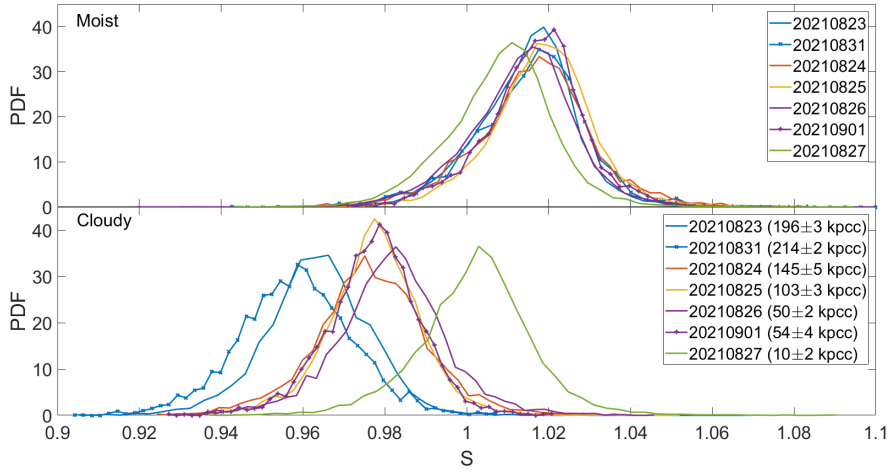

Figure 3.4: PDF of S before (top) and after (bottom) aerosol are injected into the chamber, inducing cloud formation. Here, kpcc is kiloparticles cm^{-3}.

The PDFs for the cloudy cases are shown in the bottom panel of Fig. 3.4. In every case, the introduction of aerosol particles induces a decrease in the saturation ratio, as condensation reduces the water vapor concentration and increases the temperature. As the concentration of injected particles increases, the saturation ratio shifts to lower values, though the variance of the distributions is approximately unchanged (see Table 3.1). Note that for the highest injection rates, it appears that the chamber is completely subsaturated, with even the largest positive excursions from the mean not exceeding a saturation ratio of 1 (see the blue lines in the bottom panel of Fig. 3.4). The chamber was obviously not completely subsaturated, as we did, in fact, observe a cloud under these conditions. We comment upon the possibility of an offset in our derived values of S below.

A theoretical expression for the variance of S is shown in Kulmala [33], which is:

$$\sigma^2_{S,calculated} = \left(\frac{\overline{r}}{r_s(\overline{T}}\right)^2 \left(\underbrace{\frac{\overline{r'^2}}{\overline{r^2}}}_{\text{A}} - \underbrace{\frac{2l_v}{R\overline{T}^2}\frac{\overline{r'T'}}{\overline{r}}}_{\text{B}} + \underbrace{\left(\frac{l_v}{R\overline{T}^2}\right)^2 \overline{T'^2}}_{\text{C}} \right). \tag{3.4}$$

where r' and T' are fluctuating terms, and R is the universal gas constant. The equation shows $\sigma^2_{S,calculated}$ is determined by three terms: the normalized variance of r (A), the scaled covariance of r and T (B) and the scaled variance of T (C). From our measurements of moist and cloudy conditions (See 3.1), A is the smallest term. B and C are comparable in magnitude, but on average $C > B$. Compared to the measured value of S (σ^2_S), $\sigma^2_{S,calculated}$ overestimates the variance in all cases by $\approx 10\%$. A small difference between σ^2_S and $\sigma^2_{S,calculated}$ is expected because Equation 3.4 ignores all terms with a higher order than the variance (*i.e.* the skewness and kurtosis).

When aerosols are introduced into the chamber, water vapor condenses onto aerosol particles, decreasing the mean vapor concentration, activating and growing the droplets. Water is stored in the cloud until the droplets are removed by diffusing to the walls, being sampled out of the chamber, or through gravitational settling. Settling is the dominate removal mechanism for cloud droplets in the chamber. The injection rate of aerosols has a monotonic relationship with the liquid water content (LWC) of the cloud, at least in the range of injection rates we have studied. At low injection rates, the cloud droplets have a larger mean diameter and are removed quickly by gravitational setting, resulting in a lower LWC (See Figure 3.5). As the number of of CCN increases, the droplets compete for water vapor, decreasing the

Date	8/23/2021	8/24/2021	8/25/2021	8/26/2021	8/27/2021	8/31/2021	9/1/2021
Moist							
σ_S^2 (*10^4)	1.47	2.18	1.56	1.74	1.66	1.87	1.45
$\sigma_{S,calculated}^2$ (*10^4)	1.54	2.29	1.62	1.81	1.72	1.97	1.52
A (*10^4)	1.30	1.55	1.33	1.32	1.38	1.48	1.23
B (*10^4)	1.81	1.95	2.05	1.93	2.09	2.11	2.09
C (*10^4)	2.01	1.95	2.28	2.37	2.46	2.53	2.33
Cloud							
Injection Rate (kpcc)	196±3	145±5	103±3	50±2	10±2	214±2	54±4
σ_S^2 (*10^4)	1.59	1.96	1.31	1.83	1.94	1.95	1.31
$\sigma_{S,calculated}^2$ (*10^4)	1.67	2.04	1.37	1.91	2.02	2.04	1.37
A (*10^4)	1.95	1.71	1.62	1.49	1.36	2.16	1.70
B (*10^4)	1.39	1.54	2.07	1.63	1.81	1.97	2.41
C (*10^4)	1.72	1.98	1.89	2.13	2.46	2.04	2.15

Table 3.1

The statistics for each day in moist and cloudy conditions. The variance of S derived in the same manner as the third panel of 3.1 is σ_S^2. Going from moist to cloudy conditions σ_S^2 does not appreciably change. The three different terms (in Equation 3.4 are independently calculated from r and T, where A is the water vapor variance term, B is the covariance term, and C is the temperature variance term. $\sigma_{S,calculated}^2$ is the variance of S calculated using A, B, and C with Equation 3.4. $\sigma_{S,calculated}^2$ is comparable to the measured variance, but slightly overestimates the variability of S.

mean diameter, consistent with previous results from the chamber [51].

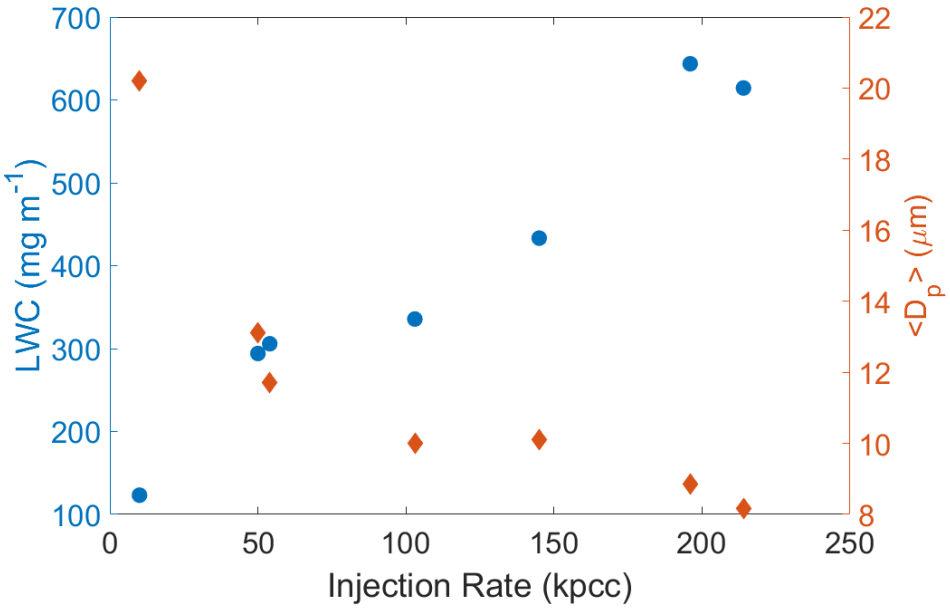

Figure 3.5: The liquid water content (blue circles) and the mean diameter (orange diamonds) for different aerosol injection rates.

Our measurements show the decrease in the water vapor concentration (N_v) corresponds to a one-to-one increase in the liquid water content of the cloud (see Fig. 3.6). It should be noted that the water vapor concentration is the same measurement as r only converted so that it uses the same units as the LWC. It is not immediately apparent why the decrease in the water vapor equals the liquid water content due to the changing fluxes from moist to cloudy conditions [76]. In steady state cloud conditions, the mass flux of water vapor to the droplets must equal the mass flux of liquid water to the walls, ceiling and floor.

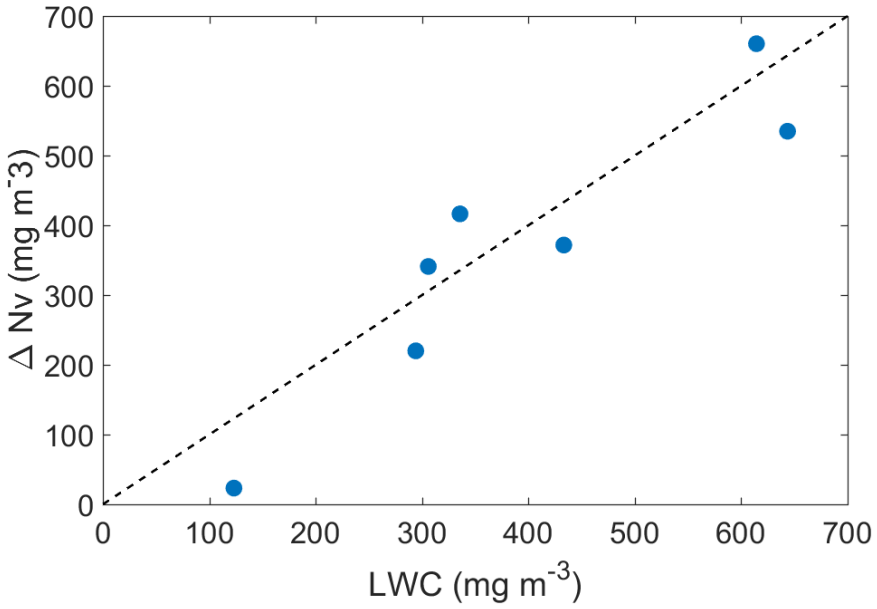

Figure 3.6: The liquid water content measured by the Welas as a function of the change in the water vapor concentration (N_v) from moist to cloudy conditions. The black dashed line is the one-to-one line, included for reference.

3.4 Discussion

As stated above, our measurements of S have an offset, which is the result of an offset in the measured temperature and/or water vapor concentration. We used an RTD to minimize the offset in temperature as described in Anderson et al [90]. The offset in the water vapor concentration is due to imperfect calibration and a drift in the zero of the LiCor [93]. To account for the offset in water vapor one might be tempted to set $\overline{S} = 1$ for the highest injection rate, and shift each other distribution accordingly. Unfortunately the variability in S allows for a cloud to form when $\overline{S} < 1$

[33]. A second possibility would shift S to the point where the fraction of S is greater than the critical supersaturation is equal to the activated fraction of NaCl. However, the timescale for a droplet to evaporate will cause the offset to be erroneously high (See Figure 4.2 and the related discussion in Chapter 4 for details). While offset in the overall mean of S is difficult to quantify, the PDFs in the top panel of Fig. 3.4 shows the offset is consistent. With the discussion in Siebert and Shaw (2017)[58] and the repeatability of the PDFs in moist conditions, we have confidence in the relative means and the variance of S.

When the environmental S deviates from the value at the droplet surface, the water vapor gradient drives condensation (or evaporation) until the droplets are in equilibrium with the environment. In a heterogeneous environment, this forcing would be expected to decrease the variability in S by decreasing S in regions of high supersaturation and increasing S in regions of low subsaturation. However, whenever there is a phase change of water, water vapor and temperature decorrelate, which increases σ_S^2. In the Π chamber the continuous forcing due to the applied temperature gradient will continuously attempt to maintain the variability seen in moist conditions. In this set of measurements, because $\sigma_{S,Cloud}^2 \approx \sigma_{S,Moist}^2$, the damping of S, decorrelation of r and T and the forcing of the chamber apparently cancel each other. In general, these feedbacks may not always cancel. If r and T are perfectly correlated in moist convection, the decorrelation due to condensation may cause $\sigma_{S,cloud}^2$ to be greater than $\sigma_{S,Moist}^2$. Alternatively, when r and T are uncorrelated or anticorrelated, the

variance may decrease when going to cloudy conditions.

While cloud droplets activate and grow in response to S, r and T must be accounted for to fully understand the distribution of S. We have shown the fluctuations in S remain even after cloud formation, which acts to broaden the cloud droplet size distribution. Increasing the concentration of aerosol particles and CCN was shown to decrease $\overline{S}$. The variability in S we have measured is likely a cause for the broadening of the cloud droplet size distribution due to the large range of droplet growth rates. Saturation ratio fluctuations are relevant for CCN activation when $\overline{S} \lesssim 0$ [54]. In a warm cloud, these regions may be relevant everywhere except the high mean supersaturation in an updraft.

Chapter 4

Enhancements in Cloud Condensation Nuclei Concentrations From Turbulent Fluctuations in Supersaturation

This chapter details how supersaturation fluctuations enhance the activation of CCN. This work is in preparation to be submitted to Nature Geoscience as a brief communication [1].

[1] Anderson, J. C., Beeler, P., Ovchinnikov, M., Cantrell, W., Krueger, S., Shaw, R. A., Yang, F. & Fierce, L. Enhancements in Cloud Condensation Nuclei Concentrations From Turbulent Fluctuations in Supersaturation. To be submitted.

4.1 Abstract

The formation of cloud droplets from aerosol particles is critical to understanding weather and climate. This process is well modeled by κ-Köhler theory under fixed humidity or uniform updrafts, but aerosol activation in a turbulent environment is not well understood. Using Lagrangian parcels driven by a Large Eddy Simulation of a laboratory chamber, we show large enhancements in aerosol activation from turbulent fluctuations in humidity.

4.2 Main

Clouds are turbulent on length scales from $\sim$1 mm to beyond the size of the cloud. A key characteristic of turbulence is the chaotic motion of the air, accelerating the mixing of air masses. Mixing of air parcels within a cloud causes fluctuations in the water vapor concentration and temperature, leading to fluctuations in water vapor supersaturation, s. Despite the fluctuations in s having been shown to activate aerosol particles when $\overline{s}$=0 [35], these fluctuations are often neglected in large-scale atmospheric models.

Earth System Models represent the globe using a collection of grid boxes that are

on the order of 100 km in each horizontal dimension. Even Large Eddy Simulation (LES) models that are designed to study cloud systems in detail use grid spacings on the order of 10–100 m, which are still too coarse to resolve the small-scale fluctuations in temperature and water vapor induced by turbulence within clouds. While LES models are used to parameterize subgrid-scale (SGS) cloud processes [43, 44, 46], these parameterizations represent spatial variability on the scale of the LES grid, not variability resulting from small-scale turbulence. Other SGS models have used Lagrangian superdroplets alongside a Linear Eddy Model to include a simplified version of the SGS variability in s [48]. Recent simulations have explored aerosol activation in a turbulent environment [91, 94].

To explore the impact of unresolved SGS fluctuations on cloud condensation nuclei (CCN) activation within warm, non-precipitating clouds, we combine Lagrangian particle tracking with a high-resolution LES of the MTU Π Chamber [79, 95]. The Π chamber is a convection cloud chamber, with a volume of 3.14 m^3, which is designed to study CCN activation, cloud droplet growth, and turbulence-induced variability in environmental properties [50]. The Π chamber LES is a modified version of the SAM model [96], with a grid spacing of 3.125 cm in each dimension. This small grid spacing is several orders of magnitude smaller than cloud-scale LES, resolving fluctuations in environmental properties at very small scales.

We simulated 10,000 Lagrangian particle (130 nm NaCl) trajectories within the Π

Chamber. The trajectory of an individual particle within the Π chamber was calculated using velocity fields from the LES, while neglecting the particle sedimentation velocity. Along the trajectory, the model tracks the temperature and water vapor mixing ratio as a function of time, which is used to compute the temporal evolution of s experienced by the particle. The temporal evolution of s for three example trajectories is shown by blue lines in Fig. 4.1. The temporal evolution of the environmental properties is then used to drive box model simulations of CCN activation and growth, shown for the three example particles by red lines in Fig. 4.1. In this study, the environment simulated by the LES was used to drive the box model simulations, while the feedback from droplet growth on environmental properties was captured by particles that were included in the LES.

As particles move through the chamber, they grow by condensation in response to the local supersaturation. To activate into a CCN, the diameter of a particle must become larger than the critical diameter ($D_{\mathrm{p,crit}}$; dashed lines in Fig. 4.1), which occurs when the particle experiences $s > s_{\mathrm{crit}}$ for enough time, where s_{crit} is the critical supersaturation. Once activated, the droplet continues to grow, as long as $s > 0$. In the case where a droplet briefly enters a region where $s > s_{\mathrm{crit}}$ and then returns to a region where $s < 0$, the size of the droplet will decrease by evaporation. A CCN-active particle will deactivate if it enters a region where $s < 0$ for a sustained period.

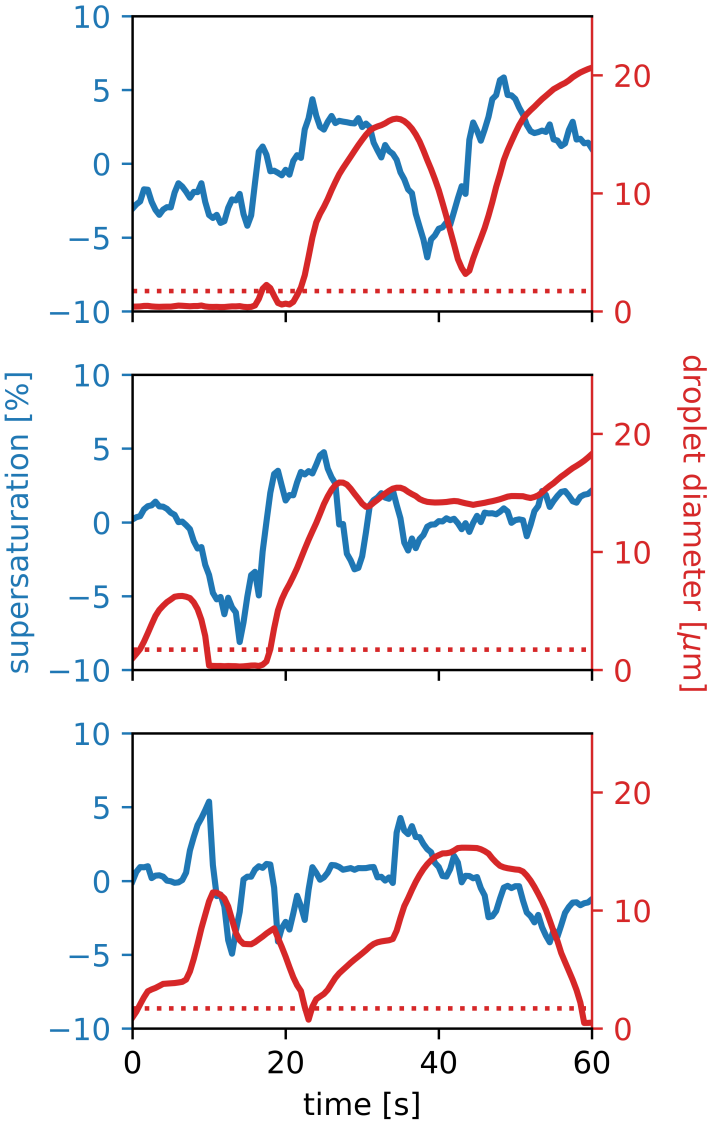

Figure 4.1: The temporal evolution of the supersaturation (blue), and the mean droplet diameter (red) along three Lagrangian parcels in the Π chamber. The dashed red lines show the critical diameter for CCN activation. In this case, $\overline{s}$=-2.7% in the chamber domain. In each panel, the particle activates and grows in response to the supersaturation fluctuations.

To explore the impact of turbulent fluctuations on droplet formation as a function of the mean environmental supersaturation across the domain, $\overline{s}$, we calculate the

activated fraction for each $\overline{s}$, for all simulated particles at a snapshot in time. The activated fraction is defined as the number of CCN=active particles (particles with $D_p > D_{\mathrm{p,crit}}$) relative to the total number of aerosol particles. The activated fraction for turbulent conditions is shown by the solid green line in Fig. 4.2. By comparison, the fraction activated under uniform s within a small domain is shown by the orange line in Fig. 4.2, which is the assumption typical of cloud-scale LES models. Given enough time at a fixed s, no particles will activate if $\overline{s} < s_{\mathrm{crit}}$, whereas every aerosol particle will activate if $\overline{s} > s_{\mathrm{crit}}$. Our results show that turbulent fluctuations in s lead to a large fraction of particles activating even when $\overline{s}$ is below 0% (100% relative humidity), which would be impossible under the uniform s approximation. This enhancement in activation from small-scale turbulent fluctuations suggests that cloud-scale LES models, as well as the global-scale parameterizations based on these LES models, will underestimate cloud droplet formation.

Although small-scale fluctuations are critical to predicting droplet formation, the environment alone is not sufficient to predict CCN activation because particles do not respond to fluctuations in s instantaneously. Instead, particles evaporate according to a characteristic timescale $\tau_{evap} = -\frac{\overline{D_p/2}^2}{2\xi_1 s}$ [97], where ξ_1 is the normalized condensation growth parameter. If $\tau_{\mathrm{evap}} = 0$, particles would instantaneously evaporate, and the heterogeneity in environmental properties alone would determine the activation fraction; this approach was applied previously in [53, 54] and is shown by the green dashed line in Fig 4.2.

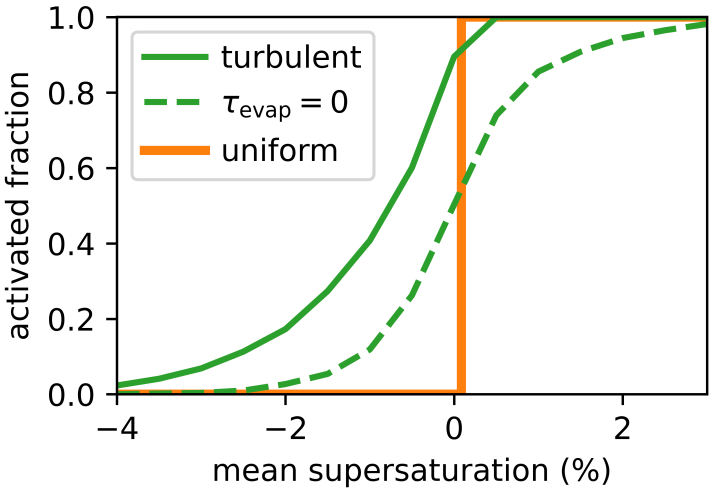

Figure 4.2: Activated fraction of droplets against the mean supersaturation in the LES volume. The activated fraction from the solid green line is determined using the droplet diameter ($D_p \geq D_{\mathrm{p,crit}}$). The dashed green line is determined by the environmental supersaturation of the droplets ($s \geq s_{crit}$). The orange line is the activated fraction where turbulent variability is neglected. When $s < 0\%$, particles activate due to fluctuations in s.

Across $\overline{s}$, we find the activated fraction is greater in our simulations than it would be if $\tau_{\mathrm{evap}} = 0$ (comparison between solid and green lines in Fig 4.2). The deviation between these two cases depends on the magnitude of τ_{evap} relative to the autocorrelation timescale of the supersaturation experienced by the droplets, τ_s. Because the sedimentation velocity is neglected, particles remain in an eddy longer than expected which artificially maintains τ_s. Using s along the ensemble of Lagrangian parcels, $\tau_s \approx 7.5$ seconds, whereas τ_{evap} is 9.9 seconds and 120 seconds for $\overline{s}$ is -1.2% and -0.2%, respectively. Because τ_{evap} is longer than τ_s, CCN remain activated for a significant period of time before evaporating. We find the instantaneous evaporation assumption underestimates the activated fraction.

In conclusion, the enhancements in aerosol activation shown here may have a large impact on the number concentration of CCN simulated by atmospheric models. CCN concentrations have long been known to affect precipitation rates and the radiative properties of clouds [3, 4, 5]. Earth system models and cloud-scale LES do not resolve the isobaric mixing of parcels with different temperatures and water vapor concentrations and, thereby, neglect the small-scale variability in s. We show that these simplifications cause models to ignore a mechanism of CCN activation and as a result, may underestimate simulated CCN concentrations. The underestimation in the CCN concentration could contribute to the large uncertainty in radiative forcing associated with aerosol-cloud interactions.

4.3 Methods

4.3.1 LES of Pi Chamber

We calculate the parcel trajectories based off of the LES output of the System for Atmospheric Modeling (SAM) [96], which has been adapted for the Π chamber [79, 95]. In this paper we report only the necessary details of the LES. The LES domain is a 2 x 2 x 1 m^3, with a grid spacing of 3.125 cm, and time step of 0.02 seconds. The top and bottom surface temperatures are set as 280 and 299 K, and both surface

are saturated with water vapor. The side wall is set to 285 K with a wall relative humidity of 78% such that the mean supersaturation without cloud droplet is about 2.5%, consistent with chamber observations. Monodisperse salt particle is injected into the chamber at a constant rate. The simulated cloud as well as the dynamic and thermodynamic fields reaches a steady state after about 5 min. The total simulation is 1 hour and the 3D velocity and scalar fields are output every 25th time step (i.e., every 0.5 seconds), which are used to calculate the motion and growth of particles in each Lagrangian trajectory.

4.3.2 Lagrangian trajectories

The particles in our box model are one way coupled with the environment. To account for errors associated with ignoring water vapor and temperature feedbacks, the Π chamber LES includes aerosol particles that interact with the environment using a spectral-bin microphysical scheme. These particles are included in the LES to ensure the water vapor and temperature fields include the effects of condensation onto particles and the evaporation of droplets. Notably, the particles in the LES are separate from our box model and are not included in our analysis.

In our box model 10,000 particles are simultaneously placed into the LES at random locations. Each aerosol particle has a dry diameter of 130nm, and the hygroscopicity

parameter (κ) is 1. The sedimentation velocity is neglected A linear interpolator is used to read the velocities, temperature, water vapor mixing ratio (wv) and s from the LES grid. The supersaturation is given by

$$s = \frac{e}{e_{sat}} - 1, \tag{4.1}$$

where e is the water vapor pressure. The saturation water vapor pressure (e_{sat}) is given by:

$$e_{sat} = 6.1094 exp\left(\frac{17.625(T - 273.15)}{(T - 30.11)}\right) \tag{4.2}$$

The position of the parcel was calculated using the initial value ordinary differential equation solver in the SciPy library with a maximum time step of 0.1s.

4.3.3 Box model simulation of droplet activation and growth

Our box model uses code adapted from Fierce et al. [98]. The differential equations for droplet growth are solved with scipy.integrate.solve_ivp. The following set of equations are used to model the growth of a particle:

$$\frac{dm}{dt} = \frac{2\pi p D_p M_w D_\infty C_T Sh}{RT} ln\left(\frac{p - e_d}{p - e}\right). \tag{4.3}$$

$$\frac{dT_p}{dt} = \left(\pi D_p^2 k_g \frac{T - T_p}{0.5 D_p} Nu + L_v \frac{dm}{dt}\right) \frac{1}{mC_p}, \tag{4.4}$$

where m is the droplet mass, p is the pressure, M_w is the molecular weight of water, e_d is the droplet water vapor pressure, D_∞ is the diffusion coefficient of water vapor, R is the universal gas constant, k_g is the thermal conductivity of air, L_v is the latent heat of vaporization, C_p is the specific heat and T_p is the temperature of the droplet. The correction factor for the diffusion coefficient (C_T), Nusselt number (Nu) and Sherwood number (Sh) are given by:

$$C_T = \left(\frac{T - T_p}{T^{\lambda-1}}\right)\left(\frac{2 - \lambda}{Tv^{2-\lambda} - T_p^{2-\lambda}}\right) \tag{4.5}$$

$$Nu = 1 + 0.3 Re^{1/2} Pr^{1/3} \tag{4.6}$$

$$Sh = 1 + 0.38 Re^{1/2} Sc^{1/3}, \tag{4.7}$$

where λ=1.6. The Schmidt number (Sc), Prandtl number, and Reynolds number (Re) are given by:

$$Sc = \frac{\nu}{D_\infty}, \tag{4.8}$$

$$Pr = \frac{C_p \mu}{k_g} \tag{4.9}$$

$$Re = \frac{|u_g - u_p| D_p}{\nu} \tag{4.10}$$

where ν is the kinematic viscosity, μ is the dynamic viscosity, u_g is the air velocity and u_p is the particle velocity. In our case $u_g - u_p = 0$

The droplet vapor pressure is calculated using κ-Köhler theory [99]:

$$e_d = e_{sat} \left(\frac{D_p^3 - D_d^3}{D_p^3 - D_d^3(1-\kappa)} \right) exp \left(\frac{4\sigma_{s/a} M_w}{R T_p \rho_w D_p} \right) \tag{4.11}$$

where $\sigma_{s/a}$ is the surface tension of the particle, and ρ_w is the density of water.

4.4 Acknowledgments

L. Fierce and M. Ovchinnikov were supported by the U.S. Department of Energy's Atmospheric System Research, an Office of Science Biological and Environmental Research program. The Pacific Northwest National Laboratory (PNNL) is operated for DOE by Battelle Memorial Institute under contract DE-AC05-76RLO1830. J.

Anderson and P. Beeler were supported by the U.S. Department of Energy, Office of Science, Office of Workforce Development for Teachers and Scientists, Office of Science Graduate Student Research (SCGSR) program. The SCGSR program is administered by the Oak Ridge Institute for Science and Education (ORISE) for the DOE. ORISE is managed by ORAU under contract number DE-SC0014664. All opinions expressed in this paper are the author's and do not necessarily reflect the policies and views of DOE, ORAU, or ORISE. The MTU coauthors were supported by U.S. National Science Foundation grants AGS-1754244 AGS-2133229. S. Krueger was supported by the National Science Foundation (managed by Michigan Technological University) under Grant AGS-2133229. F. Yang was supported by the Office of Biological and Environmental Research in the Department of Energy, Office of Science, through the United States Department of Energy Contract No. DE-SC0012704 to Brookhaven National Laboratory.

Chapter 5

Summary

Despite being a key characteristic of nearly every cloud, the effects of turbulence on small scale cloud processes are not well understood. This dissertation explored the nature these fluctuations in the saturation ratio and how those fluctuations impact CCN activation.

In Chapter 2.3, the mean flow of the Π chamber was described in dry and moist convection. In the Π chamber the LSC takes the form of a single roll, that has azimuthal oscillations. The LSC was shown to influence the local mean, variance and skewness of r, T, and S. Because of the influence on the scalar measurements, a point measurement in the center does not fully capture the spatial variability in the chamber. The LSC moves predominately along the surfaces of the chamber, however

its effects are seen in the measurements r, T and S at the center of the chamber.

Previous measurements of S in cloudy conditions measured the variability of S over large spatial scales [58] or with slow-response times [56]. The measurements shown in section 3.3 represent the first high-speed measurement of the small-scale fluctuations of S in a cloudy environment. We found S has significant variability in cloudy conditions, which can act to broaden the cloud droplet distribution. We found the variance going from cloudless to cloudy conditions does not change. Increasing the injection rate of aerosols was found to increase the liquid water content, decrease the mean droplet diameter and decrease the mean saturation ratio.

In Chapter 4 we developed a box model in order to estimate how variability in S influences the activation of aerosol particles using Lagrangian particles in a box model of the Π chamber. We found aerosol particles activate when the mean saturation ratio of the domain is subsaturated. Due to the timescale of evaporation, the distribution of s cannot be used alone to determine the fraction of activated particles. Because models tend to neglect the subgrid scale variability in S, these models may underestimate the concentration of CCN.

5.1 Future Possibilities

The results shown in Chapter 3 represent the variability of S in a cloud with a single turbulent intensity. In the atmosphere the level of turbulence is rarely constant for extended periods of time. It is likely that fluctuations of S in cloudy conditions also depend on the turbulent intensity (ΔT). This data set could be used as a benchmark case for the development of subgrid scale parameterizations.

Measurements in the chamber and simulations using the box model in Chapter 4 can be used to study preferential scavenging of aerosol particles. In Chapter 4 we show the fluctuations in S can activate CCN in regions where $s < s_{crit}$, which must change how aerosols are processed by a cloud. However, it is well known that the size and chemical composition of aerosols also determines the rate of activation [99, 100]. Introducing multiple species of aerosols into the chamber or box model domain would allow us to quantify how a diverse population of aerosol particles are removed through activation and how the cloud droplet distribution changes with different aerosol species.

References

[1] J. H. Seinfeld, C. Bretherton, K. S. Carslaw, H. Coe, P. J. DeMott, E. J. Dunlea, G. Feingold, S. Ghan, A. B. Guenther, R. Kahn, *et al.*, "Improving our fundamental understanding of the role of aerosol- cloud interactions in the climate system," *Proceedings of the National Academy of Sciences*, vol. 113, no. 21, pp. 5781–5790, 2016.

[2] T. Schneider, J. Teixeira, C. S. Bretherton, F. Brient, K. G. Pressel, C. Schär, and A. P. Siebesma, "Climate goals and computing the future of clouds," *Nature Climate Change*, vol. 7, no. 1, pp. 3–5, 2017.

[3] B. A. Albrecht, "Aerosols, cloud microphysics, and fractional cloudiness," *Science*, vol. 245, no. 4923, pp. 1227–1230, 1989.

[4] S. Twomey, "The influence of pollution on the shortwave albedo of clouds," *J. Atmos. Sci.*, vol. 34, no. 7, pp. 1149–1152, 1977.

[5] D. Rosenfeld, U. Lohmann, G. B. Raga, C. D. O'Dowd, M. Kulmala, S. Fuzzi,

A. Reissell, and M. O. Andreae, "Flood or drought: how do aerosols affect precipitation?," *science*, vol. 321, no. 5894, pp. 1309–1313, 2008.

[6] H. Morrison, M. van Lier-Walqui, A. M. Fridlind, W. W. Grabowski, J. Y. Harrington, C. Hoose, A. Korolev, M. R. Kumjian, J. A. Milbrandt, H. Pawlowska, *et al.*, "Confronting the challenge of modeling cloud and precipitation microphysics," *Journal of advances in modeling earth systems*, vol. 12, no. 8, p. e2019MS001689, 2020.

[7] F. Chillà and J. Schumacher, "New perspectives in turbulent rayleigh-bénard convection," *Eur. Phys. J. E*, vol. 35, no. 7, pp. 1–25, 2012.

[8] D. Niedermeier, K. Chang, W. Cantrell, K. K. Chandrakar, D. Ciochetto, and R. A. Shaw, "Observation of a link between energy dissipation rate and oscillation frequency of the large-scale circulation in dry and moist rayleigh-bénard turbulence," *Phys. Rev. Fluids*, vol. 3, no. 8, p. 083501, 2018.

[9] R. Krishnamurti and L. N. Howard, "Large-scale flow generation in turbulent convection," *Proceedings of the National Academy of Sciences*, vol. 78, no. 4, pp. 1981–1985, 1981.

[10] H.-D. Xi, S. Lam, and K.-Q. Xia, "From laminar plumes to organized flows: the onset of large-scale circulation in turbulent thermal convection," *Journal of Fluid Mechanics*, vol. 503, pp. 47–56, 2004.

[11] X.-D. Shang, X.-L. Qiu, P. Tong, and K.-Q. Xia, "Measured local heat transport in turbulent rayleigh-bénard convection," *Physical review letters*, vol. 90, no. 7, p. 074501, 2003.

[12] K.-Q. Xia, C. Sun, and Y.-H. Cheung, "Large scale velocity structures in turbulent thermal convection with widely varying aspect ratio," in *14th International Symposium on Applications of Laser Techniques to Fluid Mechanics*, vol. 1, 2008.

[13] H.-D. Xi, S.-Q. Zhou, Q. Zhou, T.-S. Chan, and K.-Q. Xia, "Origin of the temperature oscillation in turbulent thermal convection," *Phys. Rev. Lett.*, vol. 102, no. 4, p. 044503, 2009.

[14] E. Brown and G. Ahlers, "Large-scale circulation model for turbulent rayleigh-bénard convection," *Phys. Rev. Lett.*, vol. 98, no. 13, p. 134501, 2007.

[15] D. Funfschilling and G. Ahlers, "Plume motion and large-scale circulation in a cylindrical rayleigh-bénard cell," *Physical review letters*, vol. 92, no. 19, p. 194502, 2004.

[16] D. Funfschilling, E. Brown, and G. Ahlers, "Torsional oscillations of the large-scale circulation in turbulent rayleigh-bénard convection," *Journal of Fluid Mechanics*, vol. 607, p. 119, 2008.

[17] Q. Zhou, H.-D. Xi, S.-Q. Zhou, C. Sun, and K.-Q. Xia, "Oscillations of the large-scale circulation in turbulent rayleigh–bénard convection: the sloshing

mode and its relationship with the torsional mode," *Journal of fluid mechanics*, vol. 630, pp. 367–390, 2009.

[18] T. Vogt, S. Horn, A. M. Grannan, and J. M. Aurnou, "Jump rope vortex in liquid metal convection," *Proceedings of the National Academy of Sciences*, vol. 115, no. 50, pp. 12674–12679, 2018.

[19] M. Akashi, T. Yanagisawa, A. Sakuraba, F. Schindler, S. Horn, T. Vogt, and S. Eckert, "Jump rope vortex flow in liquid metal rayleigh–bénard convection in a cuboid container of aspect ratio," *Journal of Fluid Mechanics*, vol. 932, 2022.

[20] S. Horn, P. J. Schmid, and J. M. Aurnou, "Unravelling the large-scale circulation modes in turbulent rayleigh-bénard convection (a)," *Europhysics Letters*, vol. 136, no. 1, p. 14003, 2022.

[21] E. Brown, A. Nikolaenko, and G. Ahlers, "Reorientation of the large-scale circulation in turbulent rayleigh-bénard convection," *Phys. Rev. Lett.*, vol. 95, no. 8, p. 084503, 2005.

[22] E. Brown and G. Ahlers, "Rotations and cessations of the large-scale circulation in turbulent rayleigh-bénard convection," *J. Fluid Mech.*, vol. 568, p. 351, 2006.

[23] E. Brown and G. Ahlers, "Temperature gradients, and search for non-boussinesq effects, in the interior of turbulent rayleigh-bénard convection," *EPL*, vol. 80, no. 1, p. 14001, 2007.

[24] H.-D. Xi, Q. Zhou, and K.-Q. Xia, "Azimuthal motion of the mean wind in turbulent thermal convection," *Phys. Rev. E*, vol. 73, no. 5, p. 056312, 2006.

[25] J. C. Wyngaard, "Atmospheric turbulence," *Annual Review of Fluid Mechanics*, vol. 24, no. 1, pp. 205–234, 1992.

[26] B. Stevens, "Atmospheric moist convection," *Annual Review of Earth and Planetary Sciences*, vol. 33, no. 1, pp. 605–643, 2005.

[27] S. Salesky and W. Anderson, "Buoyancy effects on large-scale motions in convective atmospheric boundary layers: implications for modulation of near-wall processes," *Journal of Fluid Mechanics*, vol. 856, pp. 135–168, 2018.

[28] J. P. Mellado, C. C. van Heerwaarden, and J. R. Garcia, "Near-surface effects of free atmosphere stratification in free convection," *Boundary-Layer Meteorology*, vol. 159, no. 1, pp. 69–95, 2016.

[29] A. Arakawa and W. H. Schubert, "Interaction of a cumulus cloud ensemble with the large-scale environment, part i," *Journal of the atmospheric sciences*, vol. 31, no. 3, pp. 674–701, 1974.

[30] K. Fodor, J. P. Mellado, and M. Wilczek, "On the role of large-scale updrafts and downdrafts in deviations from monin–obukhov similarity theory in free convection," *Boundary-layer meteorology*, vol. 172, no. 3, pp. 371–396, 2019.

[31] O. A. Alduchov and R. E. Eskridge, "Improved magnus form approximation of saturation vapor pressure," *Journal of Applied Meteorology and Climatology*, vol. 35, no. 4, pp. 601–609, 1996.

[32] D. Lamb and J. Verlinde, *Physics and Chemistry of Clouds*. Cambridge: Cambridge University Press, 2011.

[33] M. Kulmala, Ü. Rannik, E. L. Zapadinsky, and C. F. Clement, "The effect of saturation fluctuations on droplet growth," *J. Aerosol Sci.*, vol. 28, no. 8, pp. 1395–1409, 1997.

[34] G. Sardina, F. Picano, L. Brandt, and R. Caballero, "Continuous growth of droplet size variance due to condensation in turbulent clouds," *Phys. Rev. Lett.*, vol. 115, p. 184501, Oct. 2015.

[35] C. Siewert, J. Bec, and G. Krstulovic, "Statistical steady state in turbulent droplet condensation," *Journal of Fluid Mechanics*, vol. 810, pp. 254–280, 2017.

[36] W. W. Grabowski and G. C. Abade, "Broadening of cloud droplet spectra through eddy hopping: Turbulent adiabatic parcel simulations," *Journal of the Atmospheric Sciences*, vol. 74, no. 5, pp. 1485–1493, 2017.

[37] I. Saito, T. Gotoh, and T. Watanabe, "Broadening of cloud droplet size distributions by condensation in turbulence," *Journal of the Meteorological Society of Japan. Ser. II*, 2019.

[38] N. Desai, K. Chandrakar, K. Chang, W. Cantrell, and R. Shaw, "Influence of microphysical variability on stochastic condensation in a turbulent laboratory cloud," *Journal of the Atmospheric Sciences*, vol. 75, no. 1, pp. 189–201, 2018.

[39] V. Eyring, S. Bony, G. A. Meehl, C. A. Senior, B. Stevens, R. J. Stouffer, and K. E. Taylor, "Overview of the coupled model intercomparison project phase 6 (cmip6) experimental design and organization," *Geoscientific Model Development*, vol. 9, no. 5, pp. 1937–1958, 2016.

[40] W. W. Grabowski, H. Morrison, S.-I. Shima, G. C. Abade, P. Dziekan, and H. Pawlowska, "Modeling of cloud microphysics: Can we do better?," *Bulletin of the American Meteorological Society*, vol. 100, no. 4, pp. 655–672, 2019.

[41] E. Kessler, "On the distribution and continuity of water substance in atmospheric circulations," in *On the distribution and continuity of water substance in atmospheric circulations*, pp. 1–84, Springer, 1969.

[42] W. C. Skamarock and J. B. Klemp, "A time-split nonhydrostatic atmospheric model for weather research and forecasting applications," *Journal of computational physics*, vol. 227, no. 7, pp. 3465–3485, 2008.

[43] J.-C. Golaz, V. E. Larson, and W. R. Cotton, "A pdf-based model for boundary layer clouds. part i: Method and model description," *Journal of the atmospheric sciences*, vol. 59, no. 24, pp. 3540–3551, 2002.

[44] J.-C. Golaz, V. E. Larson, and W. R. Cotton, "A pdf-based model for boundary layer clouds. part ii: Model results," *Journal of the atmospheric sciences*, vol. 59, no. 24, pp. 3552–3571, 2002.

[45] K. Thayer-Calder, A. Gettelman, C. Craig, S. Goldhaber, P. A. Bogenschutz, C.-C. Chen, H. Morrison, J. Höft, E. Raut, B. M. Griffin, *et al.*, "A unified parameterization of clouds and turbulence using clubb and subcolumns in the community atmosphere model," *Geoscientific Model Development*, vol. 8, no. 12, pp. 3801–3821, 2015.

[46] P. A. Bogenschutz and S. K. Krueger, "A simplified pdf parameterization of subgrid-scale clouds and turbulence for cloud-resolving models," *Journal of Advances in Modeling Earth Systems*, vol. 5, no. 2, pp. 195–211, 2013.

[47] F. Hoffmann, S. Raasch, and Y. Noh, "Entrainment of aerosols and their activation in a shallow cumulus cloud studied with a coupled lcm–les approach," *Atmospheric Research*, vol. 156, pp. 43–57, 2015.

[48] F. Hoffmann, T. Yamaguchi, and G. Feingold, "Inhomogeneous mixing in lagrangian cloud models: Effects on the production of precipitation embryos," *Journal of the Atmospheric Sciences*, vol. 76, no. 1, pp. 113–133, 2019.

[49] K. K. Chandrakar, H. Morrison, W. W. Grabowski, G. H. Bryan, and R. A. Shaw, "Supersaturation variability from scalar mixing: evaluation of a new

subgrid-scale model using direct numerical simulations of turbulent rayleigh–bénard convection," *Journal of the Atmospheric Sciences*, vol. 79, no. 4, pp. 1191–1210, 2022.

[50] K. Chang, J. Bench, M. Brege, W. Cantrell, K. Chandrakar, D. Ciochetto, C. Mazzoleni, L. Mazzoleni, D. Niedermeier, and R. Shaw, "A laboratory facility to study gas–aerosol–cloud interactions in a turbulent environment: The π chamber,"

[51] K. K. Chandrakar, W. Cantrell, K. Chang, D. Ciochetto, D. Niedermeier, M. Ovchinnikov, R. A. Shaw, and F. Yang, "Aerosol indirect effect from turbulence-induced broadening of cloud-droplet size distributions," *Proc. Natl. Acad. Sci.*, vol. 113, no. 50, pp. 14243–14248, 2016.

[52] K. K. Chandrakar, W. Cantrell, and R. A. Shaw, "Influence of turbulent fluctuations on cloud droplet size dispersion and aerosol indirect effects," *Journal of the atmospheric sciences*, vol. 75, no. 9, pp. 3191–3209, 2018.

[53] A. S. M. Shawon, P. Prabhakaran, G. Kinney, R. A. Shaw, and W. Cantrell, "Dependence of aerosol-droplet partitioning on turbulence in a laboratory cloud," *Journal of Geophysical Research: Atmospheres*, vol. 126, no. 5, p. e2020JD033799, 2021.

[54] P. Prabhakaran, A. S. M. Shawon, G. Kinney, S. Thomas, W. Cantrell, and R. A. Shaw, "The role of turbulent fluctuations in aerosol activation and cloud

formation," *Proceedings of the National Academy of Sciences*, vol. 117, no. 29, pp. 16831–16838, 2020.

[55] D. Niedermeier, J. Voigtländer, S. Schmalfuß, D. Busch, J. Schumacher, R. A. Shaw, and F. Stratmann, "Characterization and first results from lacis-t: a moist-air wind tunnel to study aerosol–cloud–turbulence interactions," *Atmospheric Measurement Techniques*, vol. 13, no. 4, pp. 2015–2033, 2020.

[56] H. Gerber, "Supersaturation and droplet spectral evolution in fog," *J. Atmos. Sci.*, vol. 48, no. 24, pp. 2569–2588, 1991.

[57] F. Ditas, R. A. Shaw, H. Siebert, M. Simmel, B. Wehner, and A. Wiedensohler, "Aerosols-cloud microphysics-thermodynamics-turbulence: evaluating supersaturation in a marine stratocumulus cloud," *Atmospheric Chemistry and Physics*, vol. 12, no. 5, pp. 2459–2468, 2012.

[58] H. Siebert and R. A. Shaw, "Supersaturation fluctuations during the early stage of cumulus formation," *Journal of the Atmospheric Sciences*, vol. 74, no. 4, pp. 975–988, 2017.

[59] J. L. Nowak, R. Grosz, W. Frey, D. Niedermeier, J. Mijas, S. P. Malinowski, L. Ort, S. Schmalfuß, F. Stratmann, J. Voigtländer, *et al.*, "Contactless optical hygrometry in lacis-t," *Atmospheric Measurement Techniques Discussions*, pp. 1–23, 2022.

[60] R. Pincus and M. B. Baker, "Effect of precipitation on the albedo susceptibility of clouds in the marine boundary layer," *Nature*, vol. 372, no. 6503, pp. 250–252, 1994.

[61] W. W. Grabowski and L.-P. Wang, "Growth of cloud droplets in a turbulent environment," *Ann. Rev. Fluid Mech.*, vol. 45, pp. 293–324, 2013.

[62] H. Pruppacher and J. Klett, *Microphysics of Clouds and Precipitation*. Kluwer Academic, 2nd ed., 1997.

[63] L.-P. Wang, O. Ayala, B. Rosa, and W. W. Grabowski, "Turbulent collision efficiency of heavy particles relevant to cloud droplets," *New Journal of Physics*, vol. 10, no. 7, p. 075013, 2008.

[64] A. V. Korolev and G. A. Isaac, "Drop growth due to high supersaturation caused by isobaric mixing," *Journal of the atmospheric sciences*, vol. 57, no. 10, pp. 1675–1685, 2000.

[65] K. Chandrakar, W. Cantrell, D. Ciochetto, S. Karki, G. Kinney, and R. Shaw, "Aerosol removal and cloud collapse accelerated by supersaturation fluctuations in turbulence," *Geophys. Res. Lett.*, vol. 44, no. 9, pp. 4359–4367, 2017.

[66] K. K. Chandrakar, I. Saito, F. Yang, W. Cantrell, T. Gotoh, and R. A. Shaw, "Droplet size distributions in turbulent clouds: experimental evaluation of theoretical distributions," *Quarterly Journal of the Royal Meteorological Society*, vol. 146, no. 726, pp. 483–504, 2020.

[67] R. A. Shaw, W. Cantrell, S. Chen, P. Chuang, N. Donahue, G. Feingold, P. Kollias, A. Korolev, S. Kreidenweis, S. Krueger, *et al.*, "Cloud-aerosol-turbulence interactions: Science priorities and concepts for a large-scale laboratory facility," *Bull. Am. Meteor. Soc.*, 2020.

[68] K. Chang, J. Bench, M. Brege, W. Cantrell, K. Chandrakar, D. Ciochetto, C. Mazzoleni, L. Mazzoleni, D. Niedermeier, and R. Shaw, "A laboratory facility to study gas–aerosol–cloud interactions in a turbulent environment: The Π chamber," *Bull. Am. Meteor. Soc.*, vol. 97, no. 12, pp. 2343–2358, 2016.

[69] G. Ahlers, S. Grossmann, and D. Lohse, "Heat transfer and large scale dynamics in turbulent rayleigh-bénard convection," *Rev. Mod. Phys.*, vol. 81, no. 2, p. 503, 2009.

[70] A. Belmonte and A. Libchaber, "Thermal signature of plumes in turbulent convection: the skewness of the derivative," *Phys. Rev. E*, vol. 53, no. 5, p. 4893, 1996.

[71] P. Sakievich, Y. Peet, and R. Adrian, "Large-scale thermal motions of turbulent rayleigh–bénard convection in a wide aspect-ratio cylindrical domain," *Int. J. Heat Fluid Fl.*, vol. 61, pp. 183–196, 2016.

[72] Y.-C. Xie, Y.-B. Hu, and K.-Q. Xia, "Universal fluctuations in the bulk of rayleigh–bénard turbulence," *J. Fluid Mech.*, vol. 878, 2019.

[73] Y. Liu and R. E. Ecke, "Local temperature measurements in turbulent rotating rayleigh-bénard convection," *Phys. Rev. E*, vol. 84, no. 1, p. 016311, 2011.

[74] Y.-H. He, K.-Q. Xia, *et al.*, "Temperature fluctuation profiles in turbulent thermal convection: a logarithmic dependence versus a power-law dependence," *Phys. Rev. Lett.*, vol. 122, no. 1, p. 014503, 2019.

[75] E. Brown and G. Ahlers, "The origin of oscillations of the large-scale circulation of turbulent rayleigh–bénard convection," *J. Fluid Mech.*, vol. 638, pp. 383–400, 2009.

[76] K. K. Chandrakar, W. Cantrell, S. Krueger, R. A. Shaw, and S. Wunsch, "Supersaturation fluctuations in moist turbulent rayleigh–bénard convection: a two-scalar transport problem," *J. Fluid Mech.*, vol. 884, 2020.

[77] S. K. Krueger, "Equilibrium droplet size distributions in a turbulent cloud chamber with uniform supersaturation," *Atmos. Chem. Phys.*, vol. 20, no. 13, pp. 7895–7909, 2020.

[78] M. F. Khairoutdinov and D. A. Randall, "Cloud resolving modeling of the ARM summer 1997 IOP: Model formulation, results, uncertainties, and sensitivities," *J. Atmos. Sci.*, vol. 60, no. 4, pp. 607–625, 2003.

[79] S. Thomas, M. Ovchinnikov, F. Yang, D. van der Voort, W. Cantrell, S. K.

Krueger, and R. A. Shaw, "Scaling of an atmospheric model to simulate turbulence and cloud microphysics in the pi chamber," *Journal of Advances in Modeling Earth Systems*, vol. 11, no. 7, pp. 1981–1994, 2019.

[80] X.-L. Qiu and P. Tong, "Large-scale velocity structures in turbulent thermal convection," *Physical Review E*, vol. 64, no. 3, p. 036304, 2001.

[81] X.-L. Qiu, X.-D. Shang, P. Tong, and K.-Q. Xia, "Velocity oscillations in turbulent rayleigh–bénard convection," *Physics of fluids*, vol. 16, no. 2, pp. 412–423, 2004.

[82] A. Hall and S. Manabe, "The role of water vapor feedback in unperturbed climate variability and global warming," *Journal of climate*, vol. 12, no. 8, pp. 2327–2346, 1999.

[83] J. Wyngaard, W. Pennell, D. Lenschow, and M. A. LeMone, "The temperature-humidity covariance budget in the convective boundary layer," *Journal of Atmospheric Sciences*, vol. 35, no. 1, pp. 47–58, 1978.

[84] R. C. Srivastava, "Growth of cloud drops by condensation: A criticism of currently accepted theory and a new approach," *J. Atmos. Sci.*, vol. 46, no. 7, pp. 869–887, 1988.

[85] R. A. Shaw, W. C. Reade, L. R. Collins, and J. Verlinde, "Preferential Concentration of Cloud Droplets by Turbulence: Effects on the Early Evolution of

Cumulus Cloud Droplet Spectra," *J. Atmos. Sci.*, vol. 55, no. 11, pp. 1965–1976, 1998.

[86] A. B. Kostinski, "Simple approximations for condensational growth," *Environ. Res. Lett.*, vol. 4, no. 1, p. 015005, 2009.

[87] S. K. Krueger, "Equilibrium droplet size distributions in a turbulent cloud chamber with uniform supersaturation," *Atmospheric Chemistry and Physics*, vol. 20, no. 13, pp. 7895–7909, 2020.

[88] K. K. Chandrakar, I. Saito, F. Yang, W. Cantrell, T. Gotoh, and R. A. Shaw, "Droplet size distributions in turbulent clouds: Experimental evaluation of theoretical distributions," *Quarterly Journal of the Royal Meteorological Society*, vol. 146, no. 726, pp. 483–504, 2020.

[89] H. Farahani, R. Wagiran, and M. N. Hamidon, "Humidity sensors principle, mechanism, and fabrication technologies: a comprehensive review," *Sensors*, vol. 14, no. 5, pp. 7881–7939, 2014.

[90] J. C. Anderson, S. Thomas, P. Prabhakaran, R. A. Shaw, and W. Cantrell, "Effects of the large-scale circulation on temperature and water vapor distributions in the π chamber," *Atmospheric Measurement Techniques*, vol. 14, no. 8, pp. 5473–5485, 2021.

[91] T. MacMillan, R. A. Shaw, W. H. Cantrell, and D. H. Richter, "Direct numerical

simulation of turbulence and microphysics in the pi chamber," *Physical Review Fluids*, vol. 7, no. 2, p. 020501, 2022.

[92] A. S. M. Shawon, P. Prabhakaran, G. Kinney, R. A. Shaw, and W. Cantrell, "Dependence of aerosol-droplet partitioning on turbulence in a laboratory cloud," *J. Geophys. Res.*, vol. 126, no. 5, p. e2020JD033799, 2021.

[93] LI-COR Biosciences, Lincoln, Nebraska, *LI-7500A Manual - LI-COR*, January 4, 2014.

[94] W. W. Grabowski, L. Thomas, and B. Kumar, "Impact of cloud-base turbulence on ccn activation: Single-size ccn," *Journal of the Atmospheric Sciences*, vol. 79, no. 2, pp. 551–566, 2022.

[95] F. Yang, M. Ovchinnikov, S. Thomas, A. Khain, R. McGraw, R. A. Shaw, and A. M. Vogelmann, "Large-eddy simulations of a convection cloud chamber sensitivity to bin microphysics and advection," *Journal of Advances in Modeling Earth Systems*, p. e2021MS002895, 2022.

[96] M. F. Khairoutdinov and D. A. Randall, "Cloud resolving modeling of the arm summer 1997 iop: Model formulation, results, uncertainties, and sensitivities," *Journal of the Atmospheric Sciences*, vol. 60, no. 4, pp. 607–625, 2003.

[97] M. K. Yau and R. R. Rogers, *A short course in cloud physics*. Elsevier, 1996.

[98] L. Fierce, A. J. Robey, and C. Hamilton, "Simulating near-field enhancement in transmission of airborne viruses with a quadrature-based model," *Indoor air*, vol. 31, no. 6, pp. 1843–1859, 2021.

[99] M. Petters and S. Kreidenweis, "A single parameter representation of hygroscopic growth and cloud condensation nucleus activity," *Atmospheric Chemistry and Physics*, vol. 7, no. 8, pp. 1961–1971, 2007.

[100] U. Dusek, G. Frank, L. Hildebrandt, J. Curtius, J. Schneider, S. Walter, D. Chand, F. Drewnick, S. Hings, D. Jung, *et al.*, "Size matters more than chemistry for cloud-nucleating ability of aerosol particles," *Science*, vol. 312, no. 5778, pp. 1375–1378, 2006.